Z_{DR} Column Behavior in Real and Simulated X-band Radar Observations of Potentially Tornadic Storms

JAIME L. HERRIOTT*
Department of Earth, Atmospheric, and Planetary Sciences, Purdue University, West Lafayette, Indiana
**Current affiliation: School of Meteorology, University of Oklahoma, Norman, Oklahoma*

ROBIN L. TANAMACHI
Department of Earth, Atmospheric, and Planetary Sciences, Purdue University, West Lafayette, Indiana

(Submitted 31 October 2025; in final form X)

ABSTRACT

The primary objective of this research is to characterize distinct differential reflectivity (Z_{DR}) column behavior with respect to height, intensity, and aerial coverage prior to tornadogenesis (failure) in X-band radar observations of supercells. Z_{DR} observations of three supercells observed at high spatiotemporal resolution with X-band polarimetric radar, two tornadic and one nontornadic, are examined. Similar Z_{DR} column behavior is found in all three, despite divergent outcomes with respect to tornadogenesis. Z_{DR} columns are also generated from a 30-member ensemble of simulated supercells. Height, intensity and areal extent of the simulated Z_{DR} columns are investigated just above the 0°C level. Simulated Z_{DR} column area and height both increase and Z_{DR} intensity inside the column was higher, on average, in the 5 min prior to tornadogenesis, whereas there was no appreciable change in these metrics for tornadogenesis failure. This result stands in contrast to results from our observational analysis, where there were no consistent, distinguishable changes in Z_{DR} column metrics prior to tornadogenesis versus failure. This research pinpoints Z_{DR} column metrics that can be the focus of future study, both through field observations and numerical simulations.

1. Introduction

Polarimetric weather radar allows forecasters and researchers to observe detailed microphysical processes inside of thunderstorms in near-real time (e.g., Bringi and Chandrasekar 2001, Kumjian and Ryzhkov 2008). Dual polarized radar uses the reflectivity (Z) in both the horizontal (H) and vertical (V) polarizations to calculate reflectivity values Z_H and Z_V. The difference between these two quantities ($Z_H - Z_V$) is defined as the differential reflectivity (Z_{DR}), a variable that provides information on the aspect ratio and shape of hydrometeors in the sampled volume (Seliga and Bringi 1976).

The updraft of a convective storm can loft liquid water drops above the 0°C level, where they become supercooled. These lofted raindrops are oblate in shape due to aerodynamic drag and have typical Z_{DR} values of 1 to 6 dB. In contrast, frozen hydrometeors above the 0°C level have typical Z_{DR} values of 1 to -2 dB, as they tend to be more randomly oriented or spherical (Z_{DR} ~0 dB). The contrast between relatively high-Z_{DR} oblate liquid drops extending vertically into relatively low-Z_{DR} frozen hydrometeors above the 0°C level creates a Z_{DR} column (Illingworth et al. 1987, Kumjian and Ryzhkov 2008, Romine et al. 2008).

Z_{DR} columns can be considered a proxy for updrafts (Kumjian et al. 2014). Z_{DR} columns can be used to detect the initiation of new convective storms and characterizing the evolution of convective storm updrafts (Snyder et al. 2015). For example, vertical growth (to 1 to 4 km above the 0°C level) and narrowing of the Z_{DR} column signals a rapidly intensifying updraft (Kumjian et al. 2014). As mature Z_{DR} columns are indicative of strong updrafts (Kumjian et al. 2014, Snyder et al. 2015), they can indicate conditions conducive to large and damaging hail production.

Z_{DR} columns arise from microphysical processes such as the lofting of supercooled liquid water and recycled hydrometeors within strong updrafts, and thus serve as indicators of updraft

intensity rather than direct drivers of tornadogenesis. Prior work has shown that Z_{DR} columns are closely tied to enhanced updraft strength (Kumjian et al. 2014, Snyder et al. 2015) which can contribute to vortex intensification through stretching. In convective storms, vertical vorticity is generated primarily through the tilting of horizontal vorticity associated with the environmental wind shear, followed by stretching within the updraft (Markowski and Richardson 2009; Rotunno and Klemp 1985). Low-level updraft strengthening enhances this stretching, leading to an increase in vertical vorticity near the updraft core and at the surface. Additionally, the development of a pressure deficit within the rotating updraft promotes upward acceleration via the vertical pressure gradient force, further amplifying the vertical vorticity (Fischer et al. 2024). Because Z_{DR} columns reflect the presence of strong, sustained updrafts aloft, they provide an indicator of the dynamical processes, particularly vertical acceleration and vorticity stretching, that are favorable for tornadogenesis.

There remains a gap in the understanding of changes and characteristics within Z_{DR} columns in relation to tornadogenesis. While previous research has established the importance of Z_{DR} columns in understanding storm and updraft evolution (French and Kingfield 2021, Healey and Van Den Broeke 2023, Kumjian et al. 2014, Picca et al. 2015, Van Den Broeke et al. 2020) it has been unable to conclusively link Z_{DR} column behavior and tornadogenesis. Picca et al. (2015) were the first to hypothesize that Z_{DR} columns would extend upward above the 0°C level prior to tornadogenesis reflecting the positive relationship between Z_{DR} column height and updraft strength. Using WSR-88D observations of 45 tornadic supercells, they found a strong correlation between Z_{DR} column height and changes in updraft characteristics, but only a weak correlation between Z_{DR} column height and tornadogenesis. Kuster et al. (2019) looked at whether Z_{DR} column depth could be a useful metric in tornado warning decision making for forecasters. They found this an unlikely tool to improve tornado warnings, as Z_{DR} column depth was similar in their sample of 42 tornadic and nontornadic storms observed by the KOUN polarimetric WSR-88D. Van Den Broeke (2020), studied 32 tornadic and 31 nontornadic supercells observed by operational WSR-88Ds, found that while Z_{DR} columns are larger, deeper, and less varied in tornadic storms, the small polarimetric differences due to Z_{DR} calibration drift issues (Ryzhkov et al. 2005) would make measuring Z_{DR} column changes difficult in an operational setting (Radar Observations Center DOC/NOAA 2015). French and Kingfield (2021) examined Z_{DR} column area before and during tornadogenesis in 154 tornadic supercells observed by operational WSR-88Ds, finding that Z_{DR} column area was larger in supercells that produced tornadoes rated EF3+ than in those that produced EF1 and EF2 tornadoes. They also found larger variability in Z_{DR} column area in their 154 tornadic supercells vs 44 nontornadic supercells. However, these observations were more broadly focused on tornado size and strength rather than tornadogenesis itself. Healey and Van Den Broeke (2023), using tornadic-nontornadic supercell pairs in similar environments, found that pre-tornadic storms had a larger Z_{DR} column area prior to their maximum low-level rotation than nontornadic storms and concluded that supercells with larger Z_{DR} columns are more likely to become tornadic in the immediate future.

These previous studies used observational data from S-band radars, mainly the WSR-88D. Estimating Z_{DR} column metrics with WSR-88D can be difficult due to beam spreading with height and loss of spatial resolution with increasing range from the radar (Snyder et al. 2015, Van Den Broeke 2017). The WSR-88D has relatively sparse vertical coverage above the 0°C level due to the set of discrete elevation angles in its volume coverage patterns, wherein vertical distance between successive elevation sweeps increases at longer ranges. These radars also have relatively poor temporal sampling due to volume update times of 5 to 6 minutes (Brown et al. 2005, Chrisman and DOC 2012). Supplemental Adaptive Intra-Volume Low-Level Scans (SAILS; Chrisman and DOC 2012) samples low elevation angles more rapidly, at the expense of longer revisit times at higher elevation angles, where Z_{DR} columns are generally found.

In this study, we use X-band radar observations and simulations to characterize the behavior of Z_{DR} columns prior to tornadogenesis (failure) in several tornadic and nontornadic supercells. We focus on X-band radar observations, as they generally provide higher spatiotemporal resolution than those of S-band radars (Rauber and Nesbitt 2018). By discerning distinct changes in Z_{DR} columns preceding tornadogenesis using both observations and model simulations, we hope to pinpoint Z_{DR} column features that will be the focus of future studies. We hypothesize that X-band radar

observations and simulated radar data of Z_{DR} columns will show measurable changes in height, intensity, and areal coverage in the five minutes prior to tornadogenesis that are distinct from those observed during tornadogenesis failure. The five-minute time interval is similar to the typical WSR-88D volume update time (five to six min).

2. X-band radar observations

Due to the transitory nature of severe convective storms, fixed-site S-band radars like those in the NEXRAD WSR-88D network may not have sufficiently high spatial and temporal sampling to resolve rapidly moving or changing storms (Bluestein and Wakimoto 2003). Ground-based mobile radars allow for the collection of data close to severe convective storms, even in remote locations. In addition to their proximity advantages, mobile radars tend to scan more rapidly (one to two-min volume update times), which allows the observation of rapidly changing weather phenomena and small-scale features within them. Tornadogenesis can occur on time scales of a minute or less (Bluestein and Wakimoto 2003; Pazmany et al. 2013), which is shorter than the typical volume update time for most operational radars (e.g., WSR-88D, five to six min).

Despite the proliferation of X-band mobile radars for severe storms research, we found that rapidly scanned (i.e., volume update times of <= 2 min) X-band radar observations of Z_{DR} columns through their full depth are relatively rare. Z_{DR} columns reside above the freezing level (~ 3-4 km AGL in the midlatitudes), and most radars use scanning strategies that focus on low altitudes (< 1 km AGL) where high-impact weather like microbursts, strong straight-line winds, hail, or a tornado are observed (Brown et al. 2005; Radar Operations Center and DOC/NOAA 2015; Snyder et al. 2015). Dalman et al. (2018) were able to find three robust data sets that met our criteria (i.e. volume coverage patterns that captured the full vertical extent of Z_{DR} columns above the 0°C level with temporal resolution <= 2 min).

The following subsections will describe the three cases, each of which was observed by a different X-band mobile radar, whose data were used in the observational portion of this study.

a. Case 1: Greensburg, Kansas tornadic supercell of 4 May 2007 observed by UMass X-Pol

The first ever EF5 rated tornado struck the town of Greensburg, Kansas at 0245 UTC on 4 May 2007, leaving near complete destruction and taking the lives of 11 people (Lemon and Umscheid 2008; Marshall et al. 2008; Tanamachi et al. 2012). The EF5 tornado (hereafter, "the Greensburg tornado") had a maximum damage path width of 2.74 km and a damage path length of 46.7 km (Lemon and Umscheid 2008; Marshall et al. 2008).

Dr. Howard Bluestein's research group from the University of Oklahoma used the University of Massachusetts Amherst (UMass) X-band Polarimetric Radar (UMass X-Pol; Bluestein et al. 2007) mobile radar to collect volume scans between 0132 UTC and 0234 UTC (Tanamachi et al. 2012). These scans included at least 10 tornadoes, including the Greensburg tornado and multiple cyclonic and anticyclonic satellite tornadoes during this timeframe (Lemon and Umscheid 2008). The reader is referred to Bluestein et al. (2007) for a detailed description of the radar (main characteristics are given in Table 1), and Tanamachi et al. (2012) for a detailed description of the mobile radar observations of the Greensburg tornado's parent storm and its tornadoes (Lemon and Umscheid 2008).

UMass X-Pol's volume coverage pattern during genesis of the EF5 tornado was too shallow to capture the Z_{DR} column above the 0 °C level. However, the radar operator deepened the volume later in the deployment, from 0207-0234 UTC, allowing UMass X-Pol to capture Z_{DR} column behavior during the mature phase of the EF5 tornado and genesis of both cyclonic and anticyclonic satellite tornadoes (Tanamachi et al. 2012).

Table 1. UMass X-Pol 2007 configuration (Tanamachi et al. 2012)

UMass X-Pol Characteristics	
Wavelength	3 cm
Half-Power Beam Width	1.2°
Peak Power	25 kW
Pulse Repetition Frequency	Staggered, 1.6-2.4 kHz
Max.Unambiguous Range	60 km
Max. Unambiguous Velocity	19.2 ms^{-1}
Range Gate Spacing	150 m

Max. Azimuthal Scan Rate	24° s^{-1}

b. Case 2: Luther – Carney, Oklahoma Tornadic Supercell of 19 May 2013 observed by RaXPol

During a tornado outbreak across central Oklahoma on 19 May 2013, one supercell spawned what started as an EF1 rated tornado in Fallis, Oklahoma at 2153 UTC. This tornado strengthened to an EF3 rating just south of Carney, Oklahoma at 2213 UTC. The tornado had a damage path length of 33.8 km, a maximum width of 0.8 km, and lasted 43 min (National Weather Service 2013). Sharma et al. (2021) provided in depth analysis of this storm and tornado, which occurred as part of a larger severe weather outbreak across central Oklahoma.

Dr. Howard Bluestein's research group from the University of Oklahoma captured volumetric scans of this EF3 rated tornado near Luther and Carney, Oklahoma (hereafter, "the Luther-Carney tornado"), this time using the Rapid-Scanning X-Band Polarimetric Radar (RaXPol) mobile radar (Wienhoff et al. 2018). The RaXPol is a mobile X-band (3-cm wavelength), polarimetric, Doppler radar system developed for severe weather research by Prosensing, Inc. in 2010 (Pazmany et al. 2013). RaXPol is equipped with a high-speed elevation over azimuth pedestal and a low sidelobe dual-linear polarized parabolic dish antenna mounted on a Ford F550 truck. It can complete a 10-elevation-step volume scan in roughly 20 seconds with a 180 deg s^{-1} scan rate. RaXPol utilizes frequency hopping waveforms which allows for more rapid collection of independent samples than when a single frequency is used (Pazmany et al. 2013). RaXPol, which is operated by the University of Oklahoma Advanced Radar Research Center (OU ARRC), has been used to collect high spatial and temporal resolution data in severe storms since 2011 across the U.S. central plains (Bluestein et al. 2015, Bluestein et al. 2025, Wakimoto et al. 2015).

In the present study, the data analyzed from RaXPol include the reflectivity and differential reflectivity fields collected by Dr. Bluestein's research group. The RaXPol observed Z_{DR} column behavior prior to tornadogenesis near Fallis, Oklahoma with observations continuing for an additional ten minutes after tornadogenesis.

Table 2. RaXPol configuration (Pazmany et al. 2013; https://arrc.ou.edu/radar_raxpol.html)

RaXPol Characteristics	
Wavelength	3 cm
Half-Power Beamwidth	1.2 °
Peak Power	20 kW
Pulse Repetition Frequency	1 – 8 kHz
Max. Unambiguous Range	30 to 40 km
Max. Unambiguos Velocity	30 to 38 ms^{-1}
Range Gate Spacing	7.5 m to 75 m
Max. Azimuthal Scan Rate	180° s^{-1}

c. Case 3: Greenville, Texas Nontornadic Supercell of 19 June 2019 observed by UMass Skyler

Our final observational case occurred on 19 June 2019 near Greenville, Texas. A nontornadic supercell (hereafter, "the Greenville storm", not to be confused with the Greensburg storm of 2007) was observed by Dr. Robin Tanamachi's research group from Purdue University using the UMass Skyler mobile phased array radar (Heberling and Frasier 2021).

UMass Skyler is a Raytheon dual polarization X-Band phased array radar (PAR) used by UMass MIRSL for precipitation and severe weather research. PARs use an array of transmitting elements which phase together to create a desired radiation pattern as a single antenna (Kollias et al. 2018, 2022). PAR systems, which use an active electronically scanned array for beamforming and direction, are a candidate technology to replace the WSR-88D (Weber et al. 2021). UMass Skyler's antenna array consists of 2,560 transmitting/receiving elements that are steered and configured electronically. The radiating elements are direction dependent in both phase and gain (Knappik and Frasier 2022).

For this study, the data analyzed from UMass Skyler consist of the reflectivity and differential reflectivity fields observed in the 19 June 2019 Greenville, Texas storm by Dr. Robin Tanamachi's research group from Purdue University (Tanamachi et al. 2020). The team observed a vigorously rotating updraft during deployment (Tanamachi et al. 2020) from 2225 UTC to 2235 UTC. The storm split around 2231 UTC, and no tornado formed. UMass Skyler observed the Z_{DR} column behavior for approximately eight minutes, encompassing this storm split.

Table 3. UMass Skyler 2017 configuration (Heberling et al. 2017).

UMass Skyler Characteristics	
Wavelength	3 cm
Half-Power Beam Width	1.9° Az, 2.1° El
Peak Power	125.4W
Pulse Repetition Frequency	flexible
Max. Unambiguous Range	40 km
Max. Unambiguous Velocity	18.8 ms^{-1}
Range Gate Spacing	25 m
Max. Azimuthal Scan Rate	N/A

3. Z_{DR} column detection

Building on the objective framework developed by Sharma et al. (2021) to identify and characterize Z_{DR} columns in X-band radar observations of supercells, the present study employs a closely related Z_{DR} column identification approach. Summarizing the procedure, Z_{DR} fields were first objectively analyzed to a uniform, 250-m 3D Cartesian grid using a two-pass Barnes scheme (Majcen et al. 2008). Grid sizes for each case are shown in Table 4. Additional quality control criteria were used to censor gates unlikely to contain meteorological observations. For the Greensburg, Kansas observations, gate filters were applied to exclude those with Z_H less than -10 dBZ, velocity texture (Hong and Gourley 2015) greater than 9 m s^{-1} (as this value was found to eliminate most second trip echoes), and correlation coefficient (ρ_{HV}) less than 0.7 (indicating tree blockage or non-meteorological scatterers). Owing to a data quality issue with the UMass X-Pol Greensburg ρ_{HV} data specifically (detailed by Tanamachi et al. 2013), the ρ_{HV} threshold of 0.7 is relaxed relative to higher values (0.8 or 0.9) that are usually used in polarimetric radar data analysis. Lastly, the reflectivity fields were despeckled to remove noise.

Contiguous volumes in the grid with Z_{DR} values greater than 1 dB were identified as Z_{DR} columns (Sharma et al. 2021). The Z_{DR} columns were then isolated using a convex hull implemented in the Python SciPy package (https://scipy.org/citing-scipy/, version 1.12), allowing for measurement of the columns' dimensions. Figs. 1-3 show select results of the isolation procedure for the three observed cases. Where multiple Z_{DR} columns were identified, a primary column closest to the hook echo was manually selected for study.

Table 4. Grid dimensions for each observational case used in this study.

Case	Radar	Grid Size
Greensburg, KS	UMass X-Pol	60 km x 60 km x 10 km
Luther-Carney, OK	RaXPol	45 km x 45 km x 10 km
Greenville, TX	UMass Skyler	30 km x 30 km x 10 km

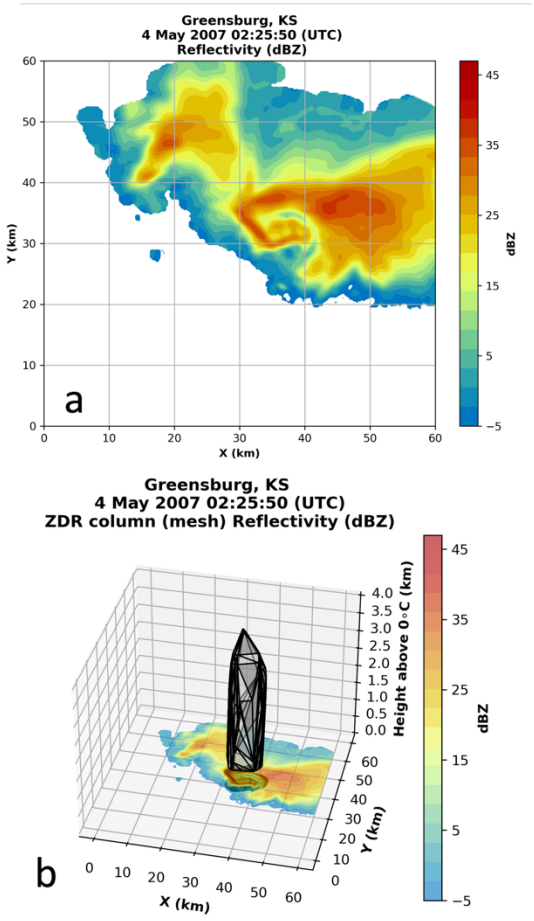

Figure 1. (a) Objectively analyzed Z_H (in dBZ) at 3.75 km ARL in the 4 May 2007 Greensburg, Kansas supercell, observed by UMass X-Pol at 0225 UTC on 5 May 2007 (Tanamachi et al. 2012). (b) Same as panel (a), but with the view expanded into 3D space and showing the Z_{DR} column in mesh with the 'shadow' (vertical projection) of the Z_{DR} column overlaid on the low-altitude reflectivity.

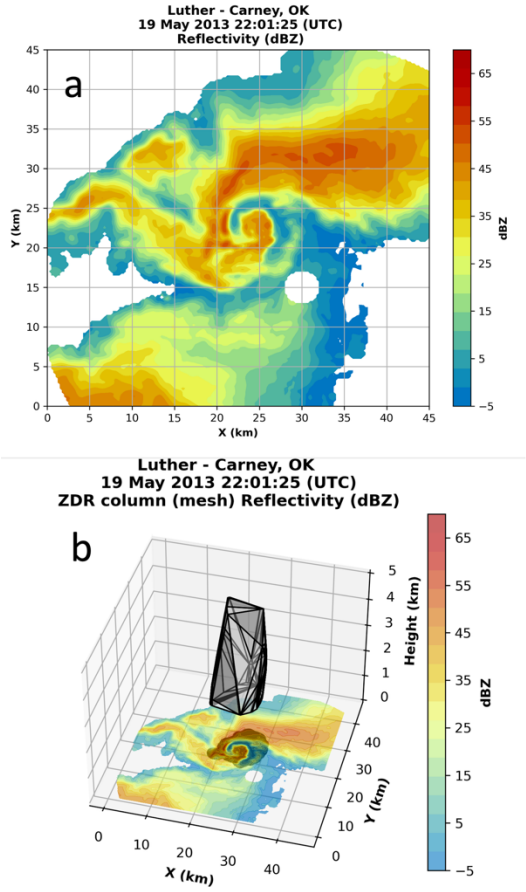

Figure 2. As in Fig. 1, but for (a) Z_H (dBZ) at 1.75 km ARL in the mature Luther – Carney, Oklahoma tornadic supercell of 19 May 2013 at 2201 UTC, derived from RaXPol radar observations (Wienhoff et al. 2018). The circular 'hole' in the reflectivity field at (30 km, 15 km) marks RaXPol's cone of silence at this altitude.

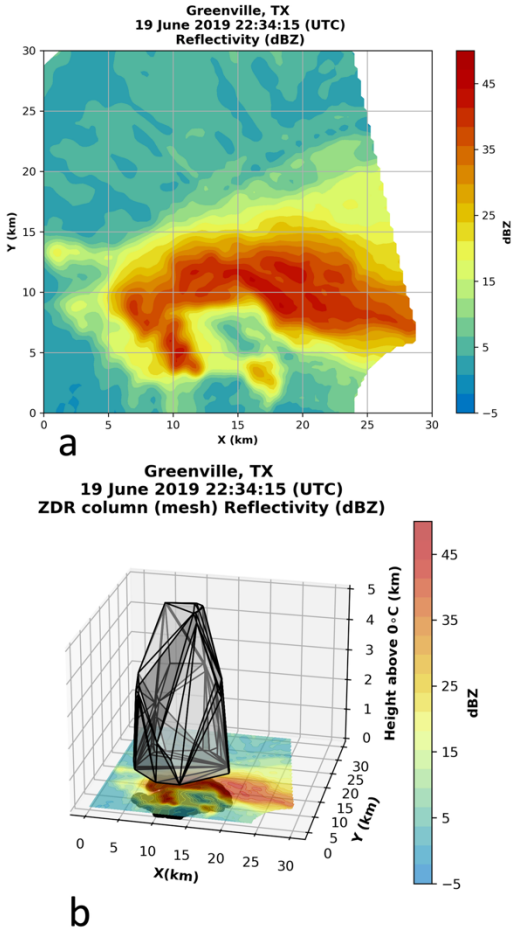

Figure 3. As in Fig. 1, but for (a) Z_H (in dBZ) at 3.75 km ARL in the Greenville, Texas nontornadic supercell of 19 June 2019 at 2234 UTC derived from UMass Skyler radar observations (Tanamachi et al. 2020).

4. Observational analysis results

We evaluated three metrics of the Z_{DR} columns:

1. Height
2. Intensity
3. Areal Coverage

These metrics were chosen as some of the most promising ones identified by other researchers for their potential prognostic utility (Snyder et al. 2015, Van Den Broeke 2020, Wilson and Van Den Broeke 2021).

a. Case 1: Greensburg, Kansas tornadic supercell of 4 May 2007 observed by UMass X-Pol

UMass X-Pol data in the Greensburg storm that spanned the full depth of the primary Z_{DR} column consisted of approximately 15 volume scans (Fig. 4). The Greensburg (EF5) tornado was ongoing throughout this period, accompanied by occasional satellite tornadoes. The Z_{DR} column area and height exhibited lagged increases occurring shortly after the formation of each satellite tornado (Figs 4, 5). Z_{DR} column height and area both increase in Figure 5 at 0213:17 UTC, at 0221:01 UTC, and again at 0228:20 UTC (although it was less pronounced; Fig. 5). The height increase at 0213 UTC is certainly artificial, as this is when the radar volume coverage pattern deepened from scanning 3° to 10° to 3° to 15° and, finally, 3° to 20° (Tanamachi et al. 2012; Table 3). The Z_{DR} column intensity (i.e., maximum Z_{DR} inside the column; Fig. 5) increased slightly before the genesis of each satellite tornado. These

metrics are consistent with periodical fluctuations in updraft intensity (i.e., a pulsing updraft), although the signal is subtle and difficult to isolate given the presence of the long-lived EF5 parent tornado. Thus, although Z_{DR} column changes occur near the times of satellite tornado formation and may be related to updraft and low-level vortex behavior, they do not provide enough evidence on their own to confirm a pulsing updraft.

Z_{DR} column area and height decreased slightly within the primary column prior to tornadogenesis. However, the pattern in these metrics is less distinct prior to genesis of each satellite tornado than it is for Z_{DR} column intensity. This result is consistent with Picca et al. (2015)'s hypothesis that the Z_{DR} column height may decrease prior to tornadogenesis in supercells due to an increase in downward pressure gradient force as the low-level mesocyclone intensifies. The increase in Z_{DR} column height and area after genesis suggest intensification of the updraft after each satellite tornado appeared.

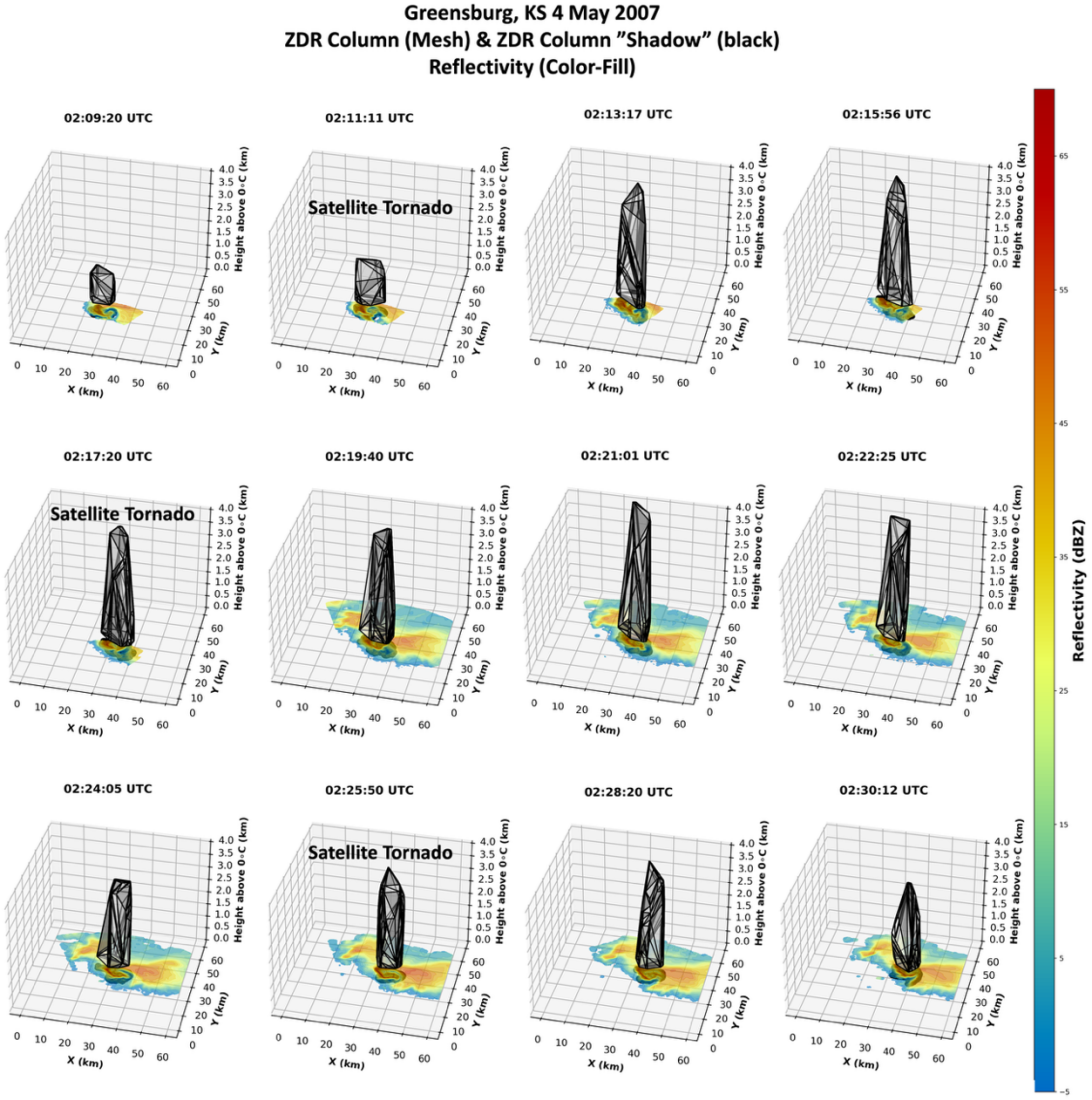

Fig. 4. Reflectivity (color fill, in dBZ), the objectively identified Z_{DR} column (mesh), and the 'shadow' of the Z_{DR} column (black) overlaid on the reflectivity for each UMass X-Pol volume scan collected from 0207:50 UTC to 0230:12 UTC on 5 May 2007. Images show the evolution of the Z_{DR} column height above 0 °C and areal coverage over time of the Greensburg, Kansas tornadic storm. The Greensburg EF-5 tornado was ongoing throughout this period; the genesis times of several satellite tornadoes are annotated.

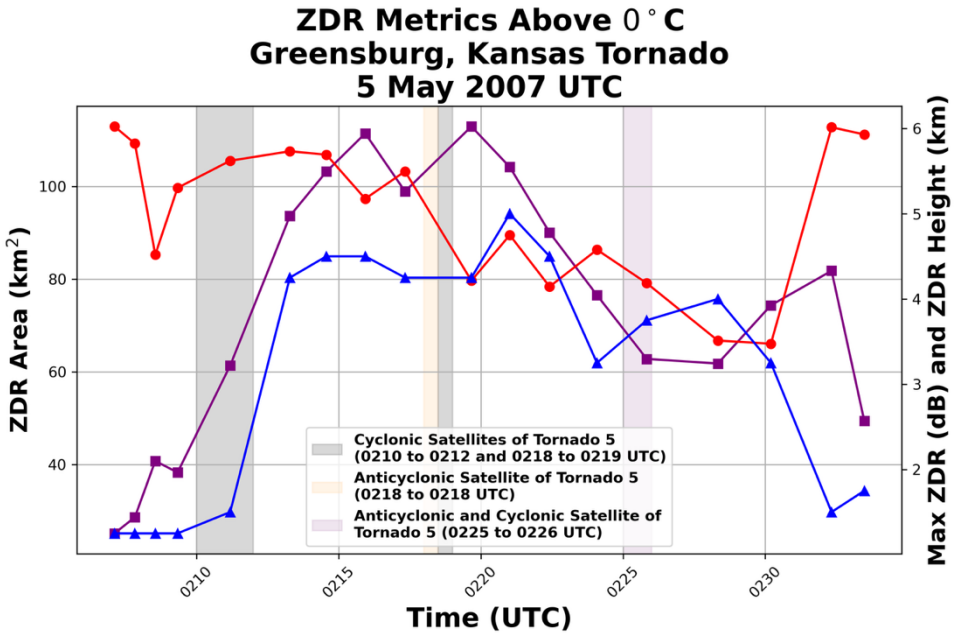

Fig. 5. Time series, from 0207 to 0233 UTC, of characteristics of the primary Z_{DR} column of the Greensburg, Kansas tornadic supercell above the 0°C level. The EF-5 rated Greensburg tornado (tornado 5 per Lemon and Umscheid, 2008; Tanamachi et al., 2012) was ongoing throughout this time frame; the times of several of its satellite tornadoes are indicated by colored shading.

b. Case 2: Luther – Carney, Oklahoma Tornadic Supercell of 19 May 2013 observed by RaXPol

The primary Z_{DR} column height (Figs. 6, 7) increased significantly, by about 1.5 km, in the three minutes prior to genesis of the Luther-Carney tornado (i.e., from 2151:01 UTC to 2153:37 UTC). This height change suggests the updraft was experiencing rapid growth just prior to tornadogenesis (Kumjian et al. 2014). This growth would not have been well resolved by a WSR-88D radar operating with a five- to six- min update time. Subsequently, the Z_{DR} column height oscillated around 3.75 km above the 0 °C level in the post-tornadogenesis period.

The Z_{DR} column area substantially increased during and after tornadogenesis, from approximately 60 km^2 to 80 km^2, as the tornado increased in strength from an EF1 rating to an EF3 rating (Fig. 7). This expansion is consistent with findings from French and Kingfield (2021). Z_{DR} column intensity generally increased in the 10-minute interval encompassing tornadogenesis, further signifying updraft intensification and growth throughout the tornadogenesis process (Fig. 7).

In contrast to Case 1, where Z_{DR} column trends were weak to difficult to distinguish owing to the presence of a long-lived parent tornado, Case 2 exhibits a more coherent increase across all Z_{DR} column metrics through tornadogenesis. This difference suggests that the relationship between Z_{DR} column behavior and tornadogenesis may be more clearly resolved in some cases than others, particularly when the signal is not obscured by confounding processes.

c. Case 3: Greenville, Texas nontornadic supercell of 19 June 2019 observed by UMass Skyler

In the Greenville, Texas nontornadic supercell, the Z_{DR} column increased in height, intensity, and area in the 1-to-5-min period preceding tornadogenesis failure (Figs. 8, 9a). Here, tornadogenesis failure refers to a supercell that exhibited characteristics typically associated with with tornadogenesis (e.g. a rotating updraft and hook echo) but did not produce a tornado despite a favorable dynamic and kinematic environment. The Z_{DR} intensity inside the column exhibited a significant increase just prior to the updraft enhancement. At 2231:22 UTC, a Z_{DR} column split was observed (Tanamachi et al., 2020) during the process of updraft intensification. The

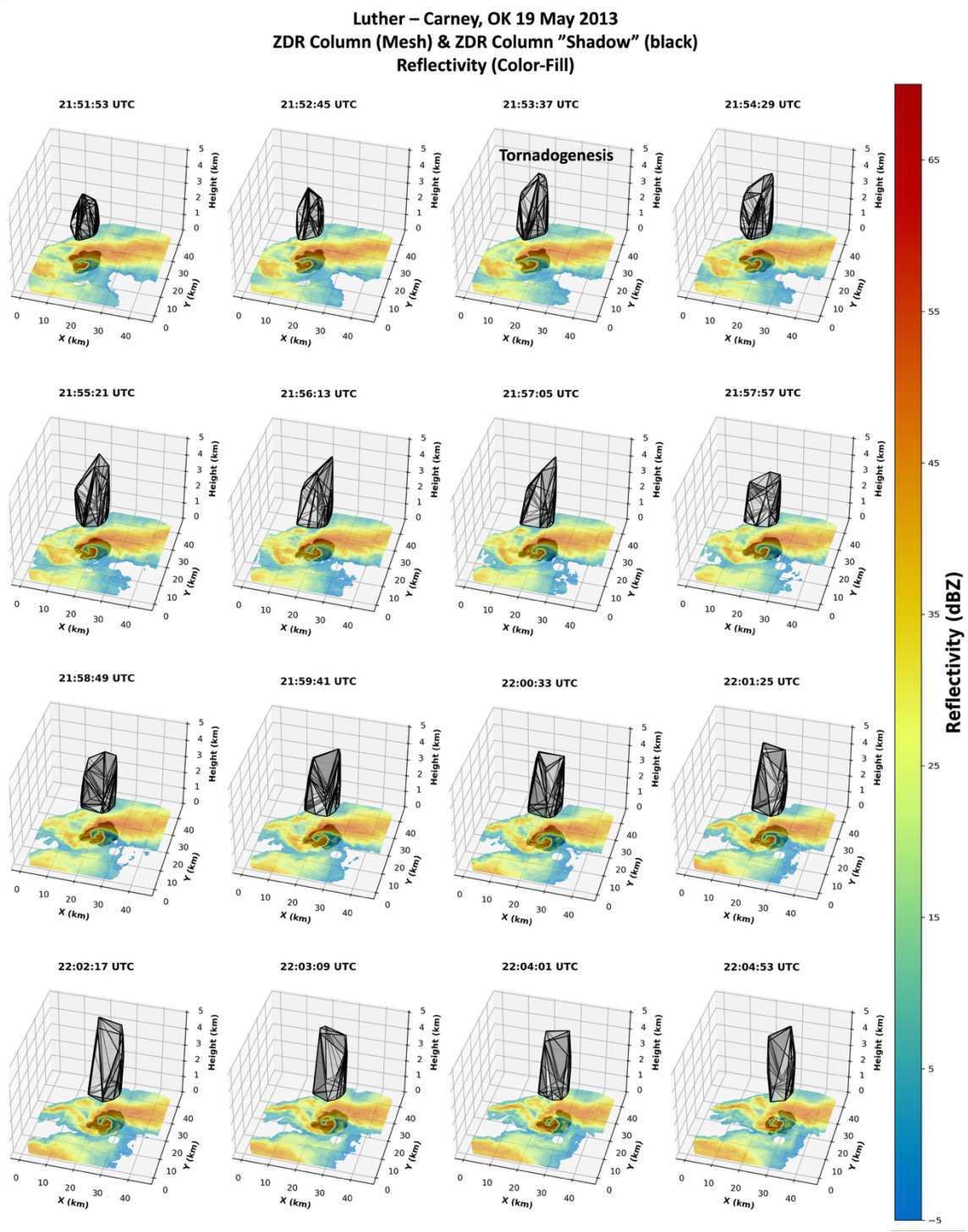

Fig. 6. As in Fig. 4, but for RaXPol volume scans collected in the Luther – Carney, Oklahoma EF-3 tornado of 19 May 2013, from 2147:32 UTC to 2204:53 UTC.

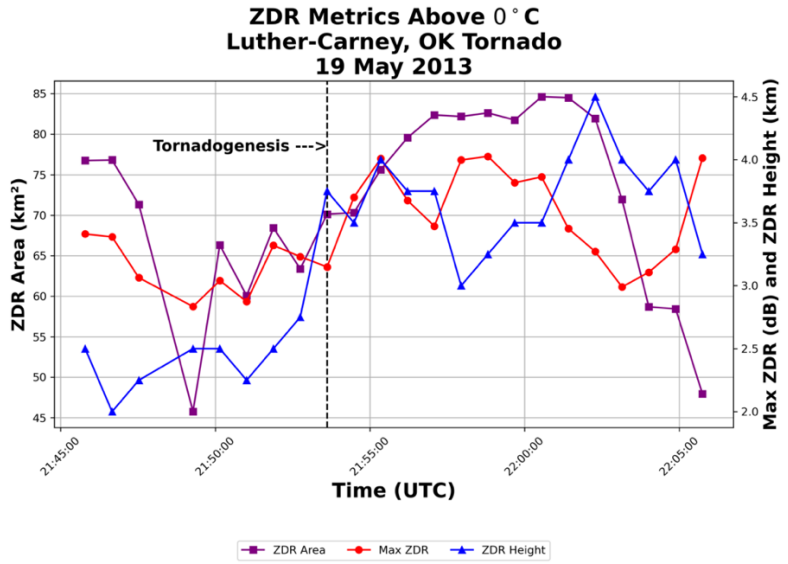

Fig. 7. As in Fig. 5, but for the primary Z_{DR} column of the Luther – Carney, Oklahoma tornadic supercell. The genesis of the Luther – Carney, Oklahoma tornado, near Fallis, Oklahoma at 2153 UTC (Sharma et al. 2021) is indicated by a dashed vertical line.

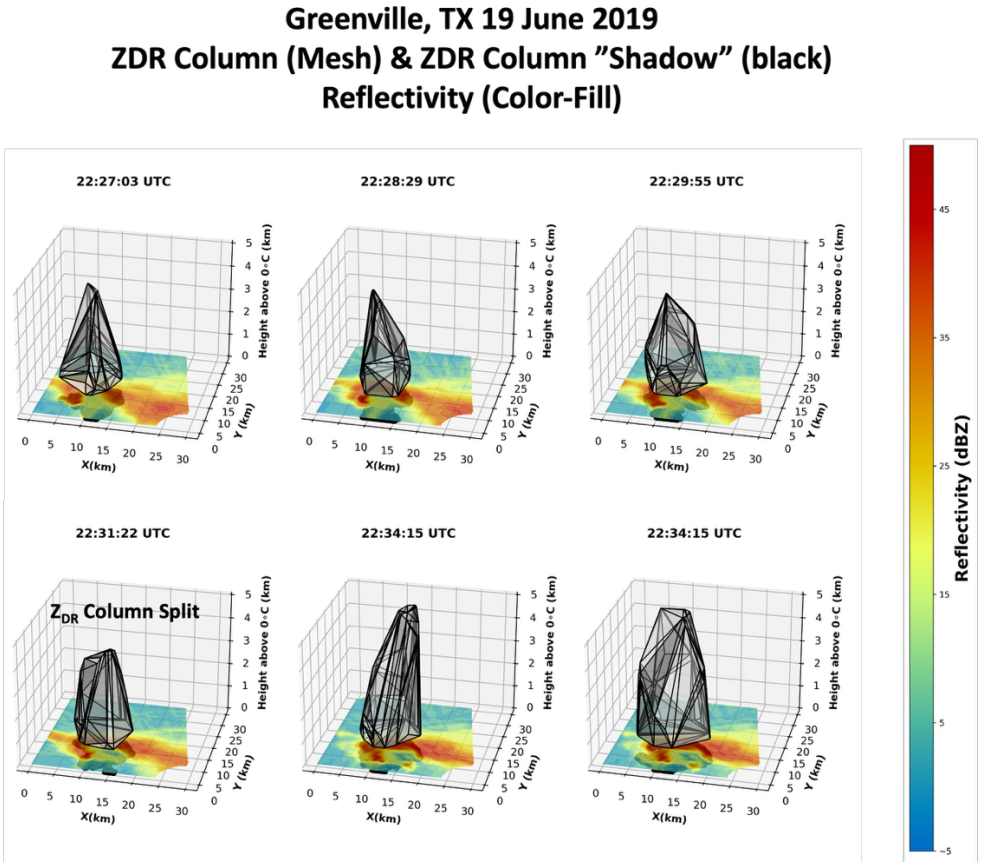

Fig. 8. As in Fig. 4, but for UMass Skyler volume scans collected in the Greenville, Texas nontornadic supercell of 19 June 2019 from 2227:03 UTC to 2234:15 UTC. Note that the Z_{DR} column split is obscured by the geometry of the convex hull.

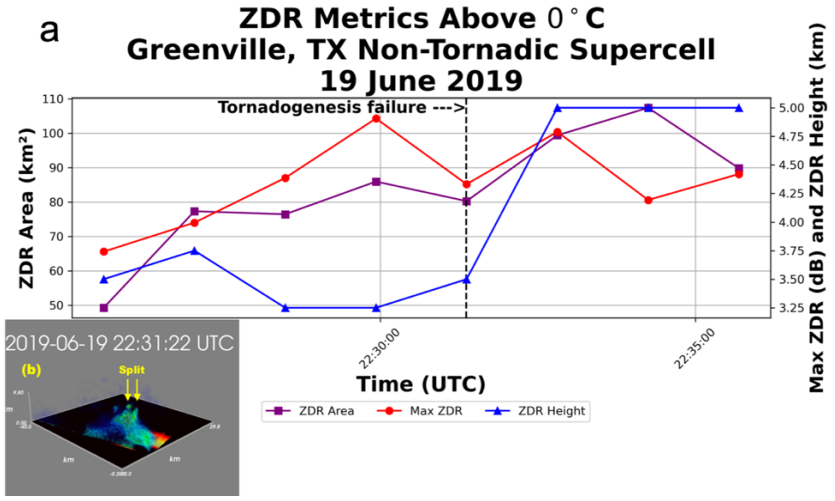

Fig. 9. (a) As in Fig. 5, but for the primary Z_{DR} column of the Greenville, Texas nontornadic supercell. The time of an apparent tornadogenesis failure and attendant Z_{DR} column split is indicated by a dashed vertical black line. (b) Volume rendering (blue) of Z_{DR} greater than 1 dB, overlaid on near-surface reflectivity, from Tanamachi et al. (2020), with the apparent supercell split annotated.

convex hull mesh (Figure 8 at 2231:22 UTC) does not show the dual peaks of the Z_{DR} columns, whereas an isosurface respresentation (Figure 9b) does. Z_{DR} intensity and Z_{DR} column area decreased in the 1 minprior to the Z_{DR} column split. However, area, height, and intensity all increase rapidly after the Z_{DR} column split. There is rapid increase in area and height after the Z_{DR} column splits, in the Z_{DR} column evolution (Figure 8 from 2231:22 UTC to 2232:48 UTC). The areal increase can be attributed to the Z_{DR} column split as the two separating columns envelop more area than the single ancestral column. As a result, the post-split increase in area likely reflects a geometric effect of the column splitting rather than a direct indication of updraft strengthening, suggesting the Z_{DR} column area may not serve as a reliable indicator of updraft evolution in this case. Furthermore, the column split indicates decreased organization of the updraft that could be the cause of tornadogenesis failure. In contrast, the Z_{DR} column height rapidly increased, suggesting updraft intensification as seen in the tornadic cases (Figure 5 and Figure 7). This result argues against our hypothesis that the Z_{DR} columns would exhibit distinct changes prior to tornadogenesis that were not present prior to tornadogenesis failure.

Table 5. Z_{DR} column metric performance for each observational case study 5 to 0 minutes prior to tornadogenesis or failure. The three entries for the Greensburg, Kansas row correspond to satellite tornadoes 6, 7 and 8 (paired), and 9 and 10 (paired) respectively (Lemon and Umscheid 2008).

Case	Height	Intensity	Area
Greensburg, KS	↔ ↓ (-0.3 km/ 3 min) ↓ (-1.8 km/ 3 min)	↑ (+1 dB/ 1 min) ↓ (-0.3 dB/ 3 min) ↓ (-0.2 dB/ 3 min)	↑ (+15 km^2/ 4 min) ↓ (-10 km^2/ 1 min) ↓ (-40 km^2/ 4 min)
Luther-Carney, OK	↑(+1.5 km/ 4 min)	↑(+0.6 dB/ 4 min)	↑(+24 km^2/ 6 min)
Greenville, TX	↑(+0.25 km/ 1 min)	↑ (+0.65 dB/ 5 min)	↑(+30 km^2/ 5 min)

5. Simulated Z_{DR} columns

The above three cases comprise the total relatively small number (to the best of the authors' knowledge) of X-band radar data sets with high spatiotemporal resolution (~100 m, ~1 to 2 min) above the 0°C level in supercells. Clearly, three cases are too few from which to draw general inferences about the behavior of Z_{DR} columns in potentially tornadic supercells. To make up for this scarcity of usable data, we generated synthetic Z_{DR} columns from high resolution numerical simulations of supercells. We coupled the model output with a polarimetric emulator (Oue et al. 2020) at X-band wavelengths to simulate radar variables. In addition to making up for the scarcity of real data cases, a simulation-based study also provides more control of the storm environment and eliminates noise and clutter that can often be present in observational X-band data.

Supercell simulations were generated using Cloud Model 1 (CM1), a cloud-resolving numerical weather forecast model (Bryan and Fritsch 2002, Bryan 2024). Our experiment setup is based on that of Coffer et al. (2017), whose ensemble samples plausible parameter spaces for tornadic and nontornadic supercells. They used CM1 Release 17 with the National Severe Storm Laboratory (NSSL) two-moment microphysics scheme (Mansell 2010; Ziegler 1985) to simulate storms for 2 hours on a 200 km x 200 km x 18 km, initially horizontally homogeneous domain. A 30-member ensemble of supercells was populated by adding small perturbations to the wind profiles of composite tornadic (15 members, denoted tor00--tor14) and nontornadic (15 members, denoted nt00-nt14) soundings created by Parker (2014) from VORTEX2 radiosonde data. Their 120-minute simulations produced a wide variety of outcomes in production of tornado-like vortices (TLVs), including "nontornadic" ensemble members that produced TLVs and "tornadic" members that did not. Moreover, a similar variety of behaviors were found related to mesocyclones, including single steady mesocyclones, multiple simultaneous mesocyclones, and shorter-lived, cyclic mesocyclones. The stochastic formulation of this experiment drew us to use it for simulation of a plausible variety of Z_{DR} column behavior.

Our experimental setup (Table 6) differed from that of Coffer et al. (2017) in that we used Release 21 of CM1 and the Morrison two-moment bulk microphysics scheme (Morrison and Milbrandt 2011) for compatibility with the polarimetric emulator (to be discussed later). A known limitation of the default CM1 namelist settings for the Morrison two-moment microphysics scheme is that resulting simulations exhibit stronger cold pools and higher surface precipitation rates than are generally observed in real supercells (Morrison and Milbrandt 2011). We performed a sensitivity experiment (not shown) on the tornadic control ensemble member (tor00) based on recommendations from H. Morrison (2025, personal communication), in which we modified the drop breakup parameter from 300 μm to 500 μm. Larger mean drop size implies drops have a smaller evaporation rate, which decreases the cold pool strength. The increase in the drop breakup threshold diameter helped to weaken the cold pool, creating a more favorable scenario for supercell longevity, structure, and tornadic potential (Dawson et al. 2013). All 30 ensemble members were run using this modification to the Morrison and Milbrant (2011) microphysical parameterization scheme.

Table 6. CM1 configuration used for this study.

CM 1 Configuration	
Domain Extent	200 km x 200 km x 18 km
Inner Mesh	50 km x 50 km x 18 km
Inner Mesh grid spacing	$\Delta x = \Delta y = 100$ m, $\Delta z \geq 20$ m
Outer Mesh	Stretching to $\Delta x = \Delta y = 3.5$ km
Horizontal Grid Size	1056 x 1056 x 115
Vertical Grid	115 levels starting at $\Delta z = 20$ m stretching to $\Delta z = 280$ m at 18 km
Pressure Solver	Klemp and Wilhelmson, 1978 time splitting, vertically implicit
Microphysics	Morrison tow-moment (Morrison and Milbrandt 2011)
Subgrid Turbulence	TKE scheme (Deardorff 1980)
Bottom Boundary Condition	Semislip
3D initialization	Updraft Nudging (Naylor and Gilmore 2012)

The full simulation domain, 200 x 200 x 18 km, contained a subdomain of 50 x 50 x 18 km to center on the supercell using an inner mesh (Table 6). We use the same metrics for simulated tornadogenesis (i.e. TLV production) defined by Coffer et al. (2017): (1) the surface vertical vorticity exceeds 0.3 s^{-1}; (2) the pressure deficit (relative to the base-state environmental sounding) within the vortex exceeds 10 hPa (or 8 hPa in the case of the nontornadic ensemble members) over a depth of at least 1 km; and (3) the instantaneous ground-relative wind speed in the vortex exceeds 35 m s^{-1}. All of these criteria needed to be concurrently present for at least 2 min for a vortex to be considered a TLV. If tornadogenesis criteria were not met, then the time of tornadogenesis failure was denoted as the time of maximum surface vertical vorticity.

CM1 does not simulate electromagnetic scattering and therefore does not produce estimates of radar variables apart from a simplified estimate of logarithmic radar reflectivity factor (the "dB*Z*" field). We applied the Cloud-resolving model Radar SIMulator (CR-SIM; Oue et al. 2020) v4.0, to the CM1 simulation output to produce simulated polarimetric radar observations. CR-SIM emulates radar observables using a forward-modeling approach that transforms precipitation microphysical quantities (mixing ratio, number concentration, and shape parameter for each hydrometeor species) in CM1 output into idealized radar variables (Oue et al. 2020). The output from CR-SIM consists of radar variables such as horizontally and vertically polarized reflectivity (Z_h and Z_v, respectively), Doppler velocity, Z_{DR}, specific differential phase, and numerous others, at each model grid point. For all 30 CM1 ensemble members (15 tornadic and 15 nontornadic) we used CR-SIM v4.0 to emulate dual polarized variables like Z_{DR} on a 501 x 501 grid point subdomain centered on the supercell. Figure 10 shows examples of CR-SIM outputs prior to being merged into CM1 output.

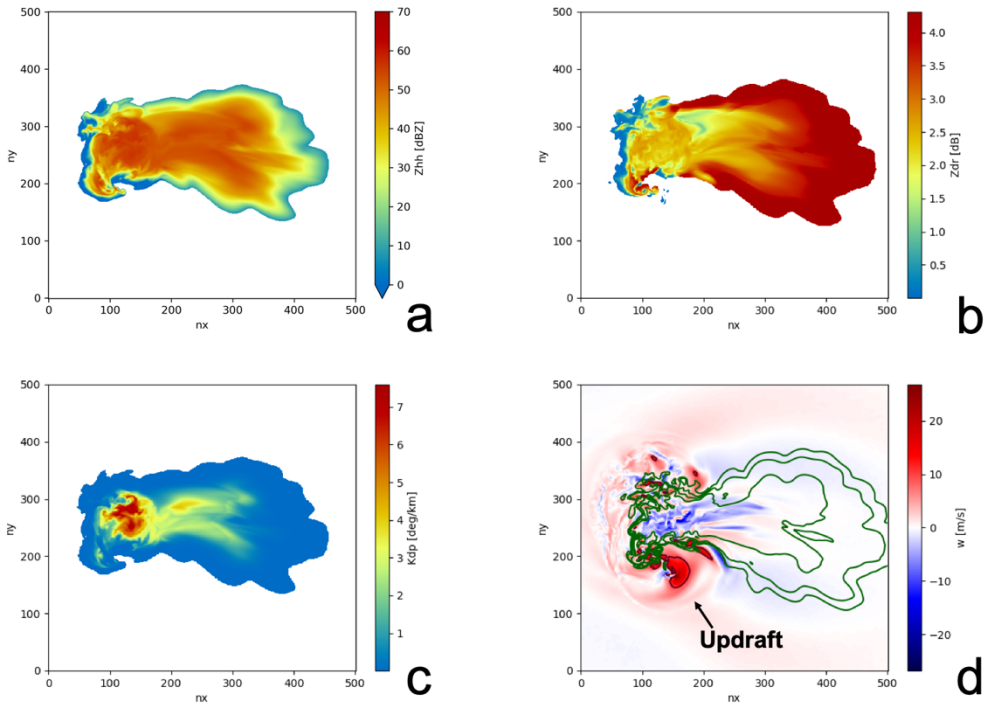

Fig. 10. CR-SIM output at the lowest model level (z = 0.01 km AGL) for (a) horizontally polarized reflectivity (in dB*Z*), (b) Z_{DR} (in dB) showing indication of high values throughout the forward flank edges consistent with size sorting issues noted in two-moment microphysics schemes (Morrison and Milbrandt 2011), (c) Specific Differential Phase (K_{DP}), and (d)vertical wind speed (w) inherited from the CM1 output from minute 28 of control sounding tor00. Horizontal axes are indicial.

An example of the resulting Z_h and Z_{DR} fields at low levels is shown in Figure 11. Panel (b) shows abnormally high values throughout the forward flank edges consistent with inadequate representation of size sorting noted in two-moment microphysics schemes (Morrison and Milbrandt 2011). However, the representation of the Z_{DR} column appears robust and realistic. Figure 12 shows a cross section of a Z_{DR} column coinciding with the edge of an updraft.

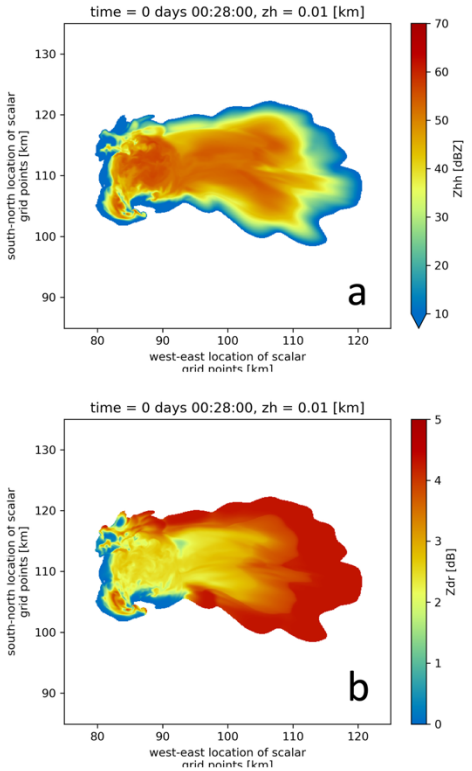

Fig. 11. Combined CM1 and CR-SIM output (a) horizontally polarized reflectivity at z = 0.01 km AGL (dB*Z*), (b) Z_{DR} (dB) from minute 28 of control sounding tor00.

X-band Z_{DR} fields were using the Cloud Resolving Radar Simulator (CR-SIM; Oue et al., 2020), a state-of-the-art polarimetric emulator on a 500 x 500 x 115 grid-point subdomain focused on the primary updraft region of the supercell. The position of the simulated radar was near the center of the simulation domain, near and south of the simulated storm's hook echo. CR-SIM output was generated for the (-5 min, +5 min) interval relative to tornadogenesis time as defined by Coffer et al. (2017)'s criteria (vorticity, pressure deficit, vortex depth). Before contiguous Z_{DR} regions were identified, Z_{DR} was masked below the 0°C level and above the -40°C level (Fig. 12) to restrict Z_{DR} column identification to mixed-phase regions. The 0°C height is where liquid water begins to freeze, and consititutes the lowest possible altitude where a Z_{DR} column can exist. Conversely, above the -40°C level, it can be safely assumed that all hydrometeors are completely frozen. With this layer defined, our identification methodology for simulated Z_{DR} columns is consistent with that used for the real Z_{DR} columns.

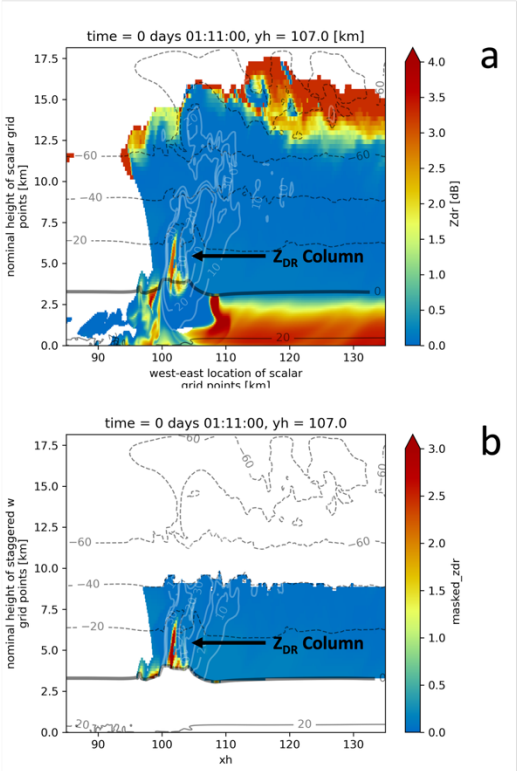

Figure 12: x – z cross section of Z_{DR} (colorfill) showing the unmasked (a) and temperature-masked (b) regions in a tornadic ensemble member. The semitransparent gray contours show the temperature in °C, with the thicker, solid gray contour showing the location of the 0°C level. The semitransparent white contours mark 10, 20, and 30 m s^{-1} vertical velocity (w) contours The spurious high Z_{DR} values at the top of the unmasked cross section are likely due to low signal levels, where very small Z_H and Z_V values introduce numerical noise and produce artificially large, noisy Z_{DR}

As with the real Z_{DR} observations, the simulated Z_{DR} columns were isolated using the convex hull method in the Python Scipy package (v1.12, Virtanen et al. 2020). Figure 13 illustrates an example of the low-level reflectivity and the isolated Z_{DR} column (mesh) above the 0°C level and shadow of the Z_{DR} column overlaid on the low-level reflectivity for a tornadic ensemble member.

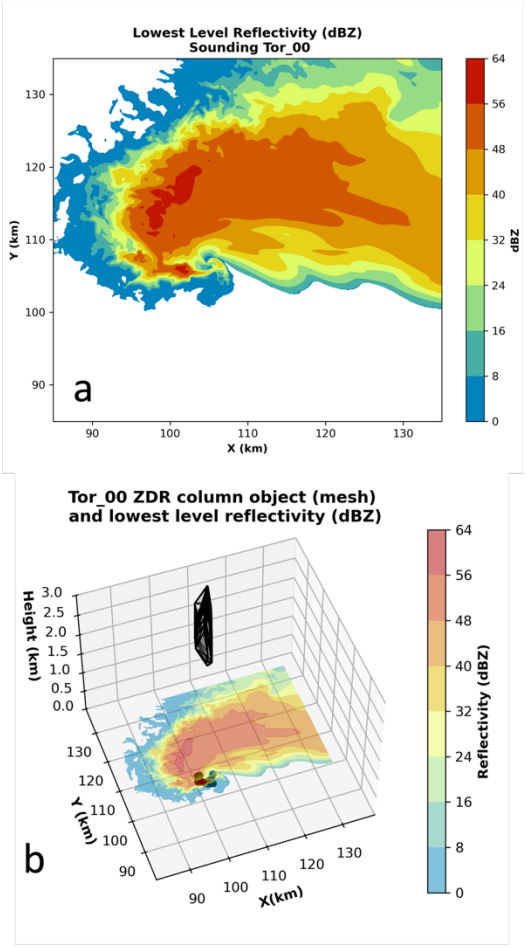

Fig. 13. (a) CR-SIM simulated horizontally polarized reflectivity (dBZ) at the lowest available model level (z = 0.01 km) from the control member (tor00) sounding at minute 81. This was the time of maximum surface vorticity for this ensemble member. (b) Same as panel (a), but showing the Z_{DR} column in mesh with the `shadow' of the Z_{DR} column overlaid on the reflectivity. Only a 50 km x 50 km subdomain of the full simulation domain is shown

6. Simulation results

For the purposes of this study, tornado-like vortex (TLV) genesis in the simulations is treated as equivalent to tornadogenesis in the observations, and hence, we use the term "tornadogenesis" for both processes. To assess potential relationships between tornadogenesis and Z_{DR} column behavior in the simulated ensemble of supercells, we applied the criteria of Coffer et al. (2017), which include thresholds for vertical vorticity, pressure deficit, and vortex depth. If these three criteria occurred simultaneously for a period longer than 2 minutes, tornadogenesis was said to have occurred. TLVs identified during the first 30 minutes of the simulation were excluded from further analysis, as this period was considered model spin-up, during which the model adjusted from its initial conditions and the simulated convective dynamics were not yet fully developed. If a simulation produced vortices that approached but did not meet the tornadogenesis thresholds (section 5), tornadogenesis failure was said to have occurred. In these cases, the time of tornadogenesis failure was taken as the time of maximum surface vertical vorticity (Coffer et al. 2017). Thus, tornadogenesis (TLV) failure represents a near-miss scenario rather than a complete absence of vortex development. Because no TLVs were detected in any of the nontornadic members that met Criterion 2, the required pressure-deficit threshold was relaxed to 8 hPa for all nontornadic members. Similar to the findings of Coffer et al. (2017), the "tornadic" and "nontornadic" classifications of the initial soundings did not necessarily correspond to the simulated outcomes with respect to TLV production. In other words, some ensemble members initialized with "nontornadic" soundings produced one or more TLVs, while some initialized with "tornadic" soundings did not. Moreover, some ensemble members produced multiple tornadogenesis (failure) events.

Following the spin-up period, each ensemble member was categorized according to TLV behavior (Fig. 14) as:

1. **No TLV**: No TLV detected during the entire 90-min simulation.
2. **TLV during spin-up**: TLV detected during simulation minutes 0 to 30.
3. **TLV failure**: TLV genesis failure during simulation minutes 30 to 90.
4. **Single TLV producing**: One TLV detected during simulation minutes 30 to 90.
5. **Long-lived TLV producing**: One TLV lasting longer than 10 minutes during simulation minutes 30 to 90
6. **Multiple TLV producing**: Multiple TLVs produced during simulation minutes 30 to 90.

We included only ensemble members that produced either (a) at least one TLV after the 30-min spin-up period, or (b) a TLV failure event during the same period. Ensemble members that produced TLVs only during the spin-up period, or that did not exhibit TLV development, were

Fig. 14: Outcomes of each tornadic and Nontornadic ensemble member.

excluded. After applying these criteria, the analysis included 10 tornadic ensemble members (0, 1, 3, 4, 5, 6, 10, 11, 12, 13) and 9 nontornadic ensemble members (0, 1, 3, 4, 7, 9, 10, 11, 13). Here, the included nontornadic members correspond to cases exhibiting TLV failure, rather than complete absence of vortex development.

a. Simulated Z_{DR} column analysis

We used CR-SIM to produce synthetic Z_{DR} fields for the 19 ensemble members selected for the next stage of study.

In the three observational case studies (Section 4), Z_{DR} columns encompassed the primary updrafts of their respective storms (Figures 4, 6, and 8). We identified many more candidate Z_{DR} objects above the freezing level in our simulations than were found in the observed supercell cases. On occasion, multiple candidate Z_{DR} objects were detected within the updraft region of the simulated supercell. When this occurred, the Z_{DR} column of interest was taken to be that with highest mean internal vertical velocity (i.e., collocated with the updraft).

Once our Z_{DR} object within the region of interest was identified, the following Z_{DR} column metrics were calculcated for an 11-min window centered on each tornadogenesis (failure) event:

1. Height: The vertical extent of the convex hull enclosing the identified Z_{DR} column.
2. Intensity: The maximum value of Z_{DR} within the column.
3. Areal Coverage: The projected area of the 3D convex hull on the x-y plane.

Fig. 15 is an example of the simulated Z_{DR} column evolution over time taken from tornadic ensemble member 04 (tor04). Overall, the simulated Z_{DR} columns were smaller compared to the observed Z_{DR} columns (Section 4). We attribute this difference to an apparent artificial upper limit on mean drop size within the two-moment Morrison microphysics scheme. The default two-moment Morrison scheme uses a ~2.8-mm mean diameter for the drop distribution, corresponds to ~4.5 dB according to Beard and Chuang (1987). Additionally, the Morrison and Milbrandt (2011) two-moment scheme incorporates a drop breakup parameterization. As previously mentioned, we adjusted the drop breakup parameter from the default 300 μm to 500 μm based on advice (H. Morrison 2024, personal communication). This adjustment allows larger mean drop sizes to persist before breakup, which helps constrain cold pool production. However, even with this adjustment, the synthetic Z_{DR} column intensity never seemed able to exceed 4.5 dB. In contrast, the observed Z_{DR} columns exhibited maximum Z_{DR} as high as 6.0 dB in UMass X-Pol observations of the Greensburg, Kansas storm (Fig. 5) and as high as 4.9 dB in UMass Skyler observations of the Greenville, Texas storm (Fig. 9). Clearly, the precipitation microphysics scheme still struggled to replicate real-world complexities of drop size distributions within storms. This issue will need to be addressed in future studies. We proceed nonetheless, focusing on the *trends* in Z_{DR} intensity, rather than the specific values.

Overall Z_{DR} column behavior is exemplified by ensemble member tor04 (Fig. 15). Ensemble member tor04 produced a TLV that began at t = 74 min and lasted roughly five min. Its primary Z_{DR} column increased in height and areal coverage prior to TLV genesis and continued to do so after TLV genesis. The Z_{DR} column decreased in height and areal coverage around the 79-min mark, indicating the updraft had also begun to weaken just prior to the TLV dissipation.

However, similar behavior was also observed in the nine nontornadic ensemble members examined (Table 7). Fig. 16 shows typical Z_{DR} column evolution from a nontornadic ensemble member (nt03). This case behaved like the tornadic cases, with the Z_{DR} column height and area increasing prior to TLV genesis failure. However, the column shrank at the tornadogenesis failure timestep and quickly

became smaller in area, becoming unidentifiable five minutes after TLV genesis failure. This behavior was consistent with the tornadic members in that their Z_{DR} column metrics increased (on average) prior to tornadogenesis, but those metrics quickly diminished at or shortly after TLV genesis failure. This result indicates weaker updrafts overall in the nontornadic members, as Z_{DR} column height correlates with vertical velocity (Kumjian et al. 2014). This result is perhaps unsurprising, as Parker (2014)'s nontornadic composite sounding had slightly less surface-based CAPE (2377 J kg^{-1}) than the tornadic composite sounding (2755 J kg^{-1}) (Coffer and Parker 2018).

Fig. 17 shows the height and areal coverage of the Z_{DR} column for each TLV-producing tornadic ensemble member at the time of tornadogenesis. Fig. 18 shows the height and areal coverage of the Z_{DR} column for each nontornadic ensemble member at the time of tornadogenesis failure. Z_{DR} columns associated with tornadogenesis failure are, overall, smaller and less developed than the Z_{DR} columns associated with tornadogenesis.

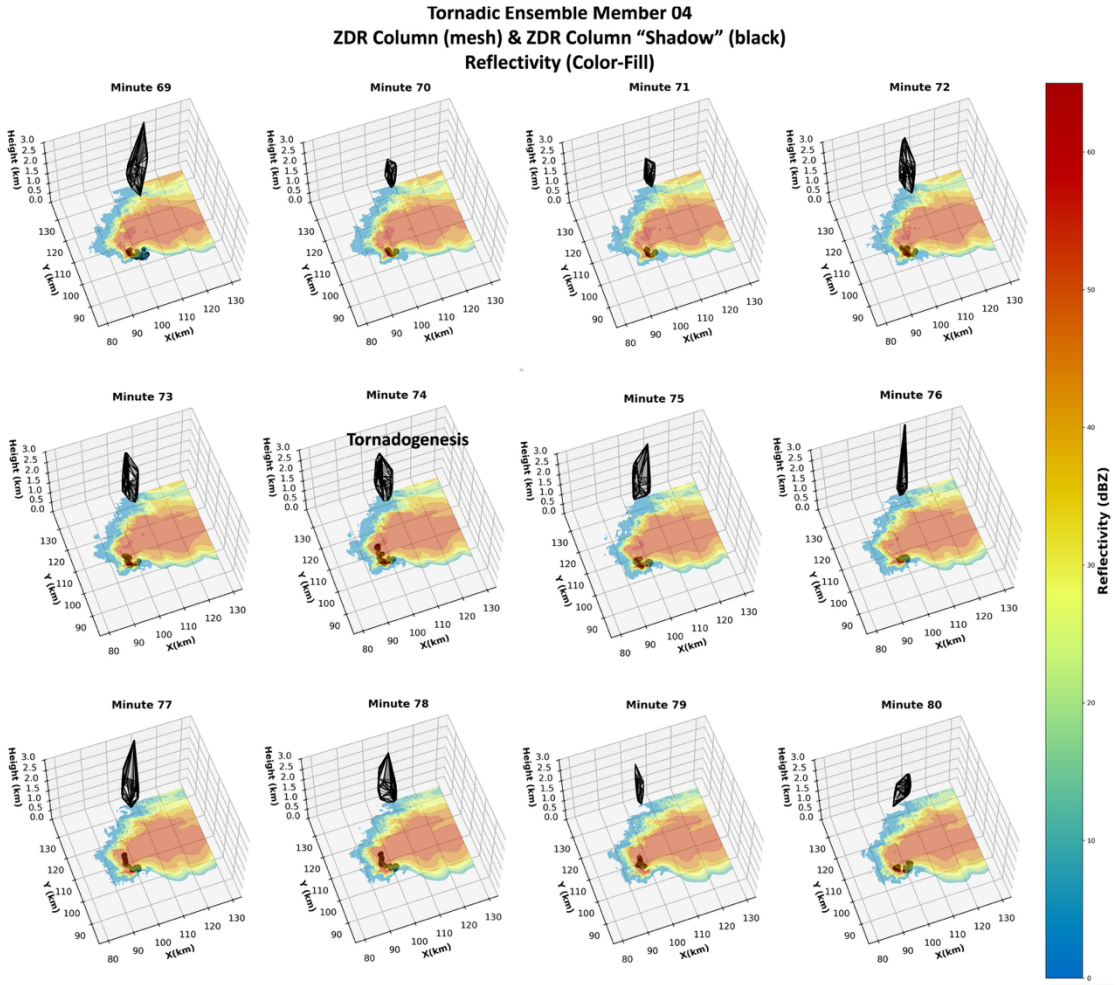

Fig. 15: Simulated reflectivity (color fill), the Z_{DR} column (mesh), and the 'shadow' of the Z_{DR} column (black) overlaid on the reflectivity from minutes 69 to 80 of the tornadic ensemble member 04. Images show the evolution of the Z_{DR} column height above 0 °C and areal coverage over time

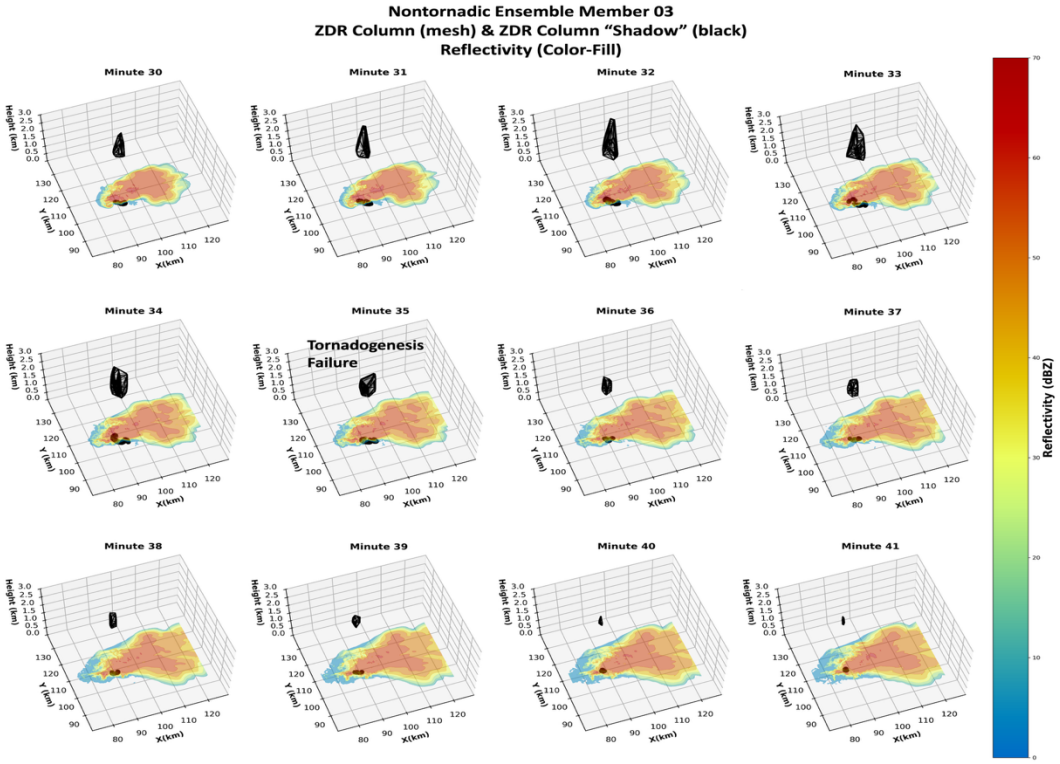

Fig. 16: As in Fig. 15, but for minutes 30 to 41 of the nontornadic ensemble member 03.

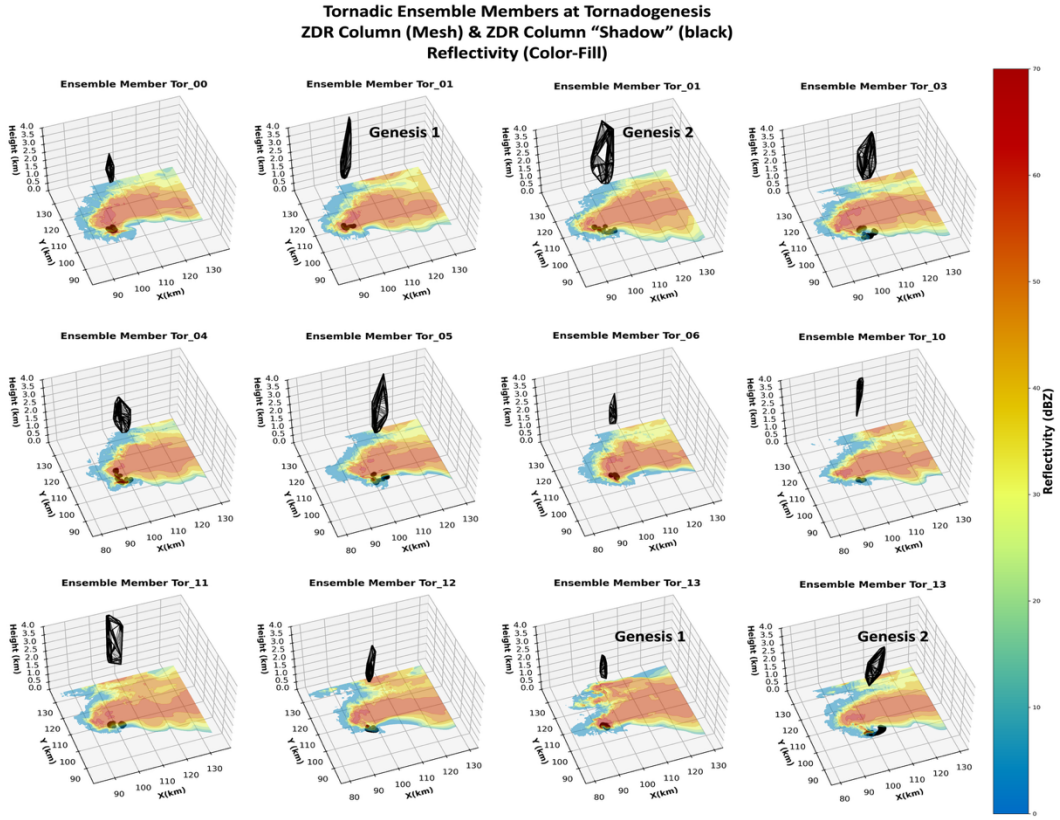

Fig. 17: As in Fig. 15, but for all 12 TLV-producing tornadic ensemble members at their respective tornadogenesis times.

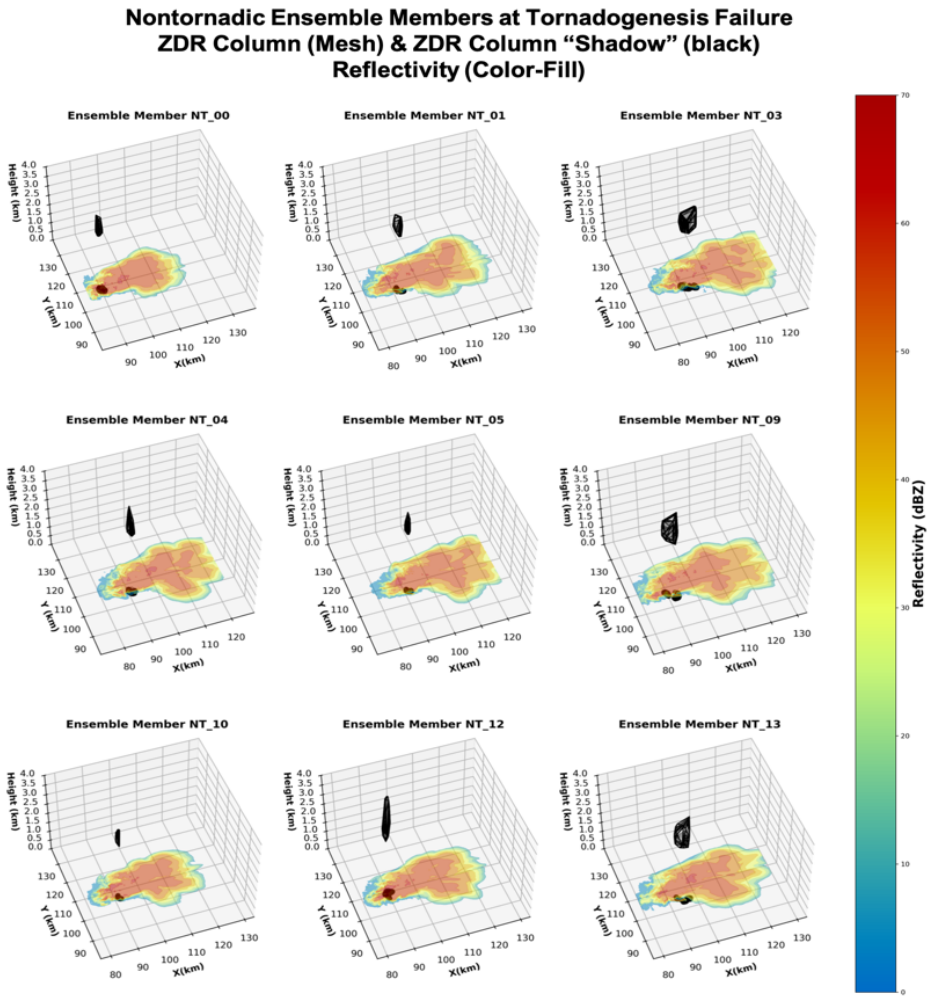

Fig. 18: As in Fig. 17, but for all nine nontornadic ensemble members at their respective tornadogenesis failure times.

To quantify the relationship between height and area of the Z_{DR} columns observed in tornadic and nontornadic ensemble members at tornadogenesis (failure), we calculated the aspect ratio. Using the height and area metrics obtained from the convex hull, aspect ratio was calculated as:

$$\text{Aspect Ratio} = \frac{H^2}{A}$$

Apart from one single outlier amongst the nontornadic Z_{DR} columns, the tornadic Z_{DR} columns all had higher aspect ratios than the nontornadic Z_{DR} columns (Fig. 19), indicating that all of the tornadic Z_{DR} columns were relatively tall and narrow compared to the nontornadic Z_{DR} columns at tornadogenesis (failure), as can be seen in Figure 17. The tornadic Z_{DR} columns also had a wider range of aspect ratios compared to the nontornadic Z_{DR} columns (Fig. 19).

Because the vertical velocity (w) field is available from these simulations, it is possible to characterize the updraft strength inside each Z_{DR} column object. The higher aspect ratios for tornadogenesis-associated Z_{DR} columns are consistent with their enhanced vertical velocity (Fig. 20), potentially causing vertical vortex stretching. This result is consistent with RaXPol observations of Z_{DR} column behavior during tornadogenesis in the Luther – Carney, Oklahoma case (Section 4b), where tornadogenesis was preceded by rapid intensification of the updraft. Conversely, shorter and squatter Z_{DR} columns at tornadogenesis failure (Fig. 18, 19) contained relatively low vertical velocities (Fig. 20) which would not allow for as much vortex stretching and intensifying rotation needed for tornadogenesis.

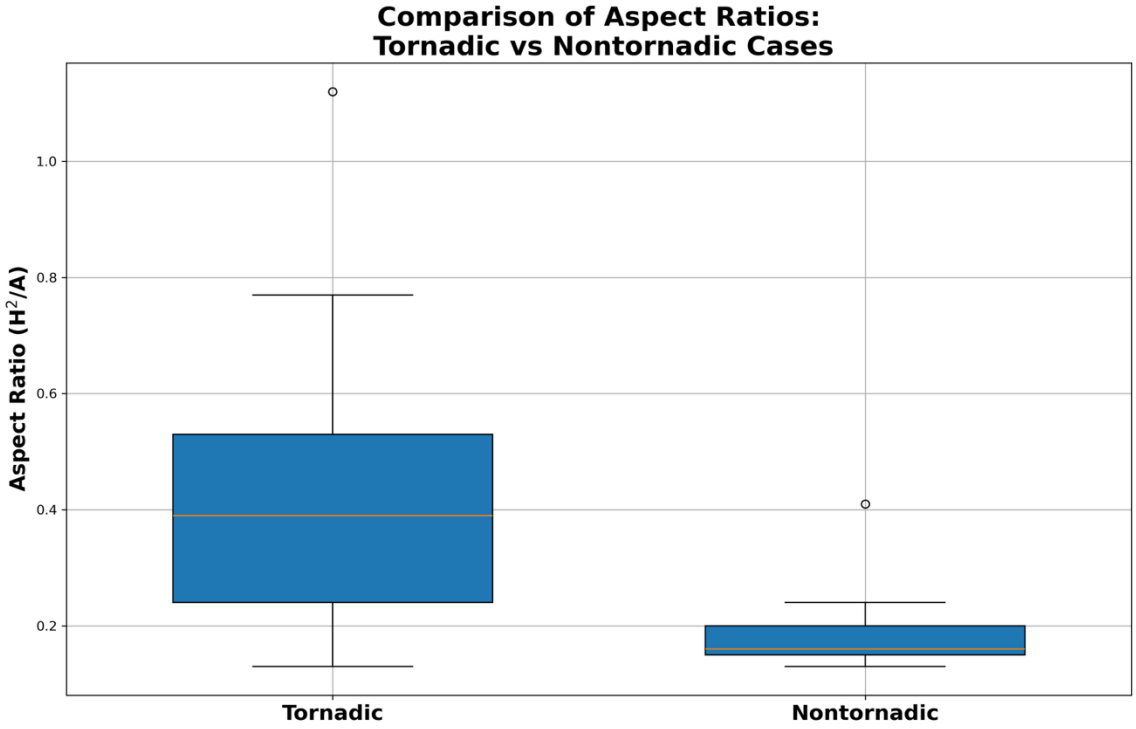

Fig. 19: Box and whisker plots of the aspect ratio (H^2/A) of the Z_{DR} column of tornadic and nontornadic members at tornadogenesis and tornadogenesis failure, respectively. Higher aspect ratios indicate relatively tall, narrow Z_{DR} columns.

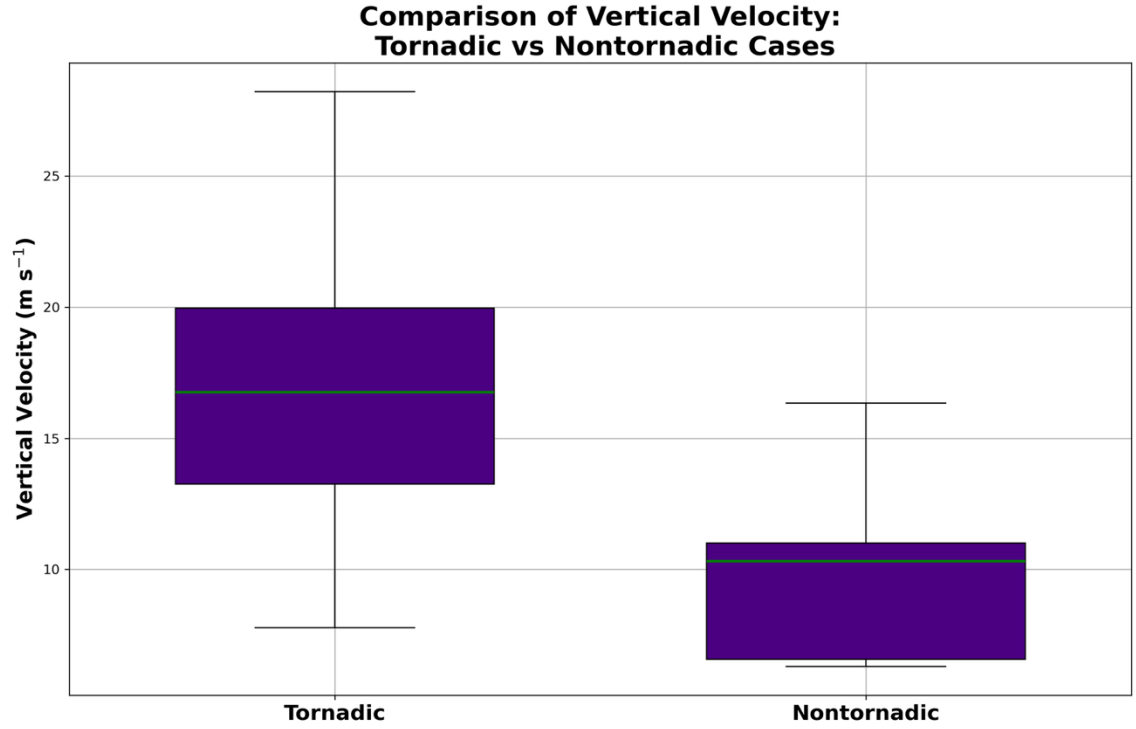

Figure 20: Box and whisker plots of the vertical velocity inside the Z_{DR} columns of tornadic ensemble members and nontornadic members at tornadogenesis and tornadogenesis failure, respectively.

b. Simulated Z_{DR} column trends

We also examined the Z_{DR} column mean trends in the five minutes prior to tornadogenesis (failure) until the five minutes after tornadogenesis (failure) for the 10 tornadic and nine nontornadic ensemble members. Three of our tornadic ensemble members had two tornadogenesis events apiece, giving us 13 tornadogenesis events. None of the nontornadic ensemble members had multiple tornadogenesis failure events.

First, we examined trends in the intensity (or internal maximum Z_{DR}) of the Z_{DR} column relative to tornadogenesis (failure) time (Figs. 21 and 22). Z_{DR} in the tornadic ensemble members appears to have an artificial upper bound around 4.5 dB. The Z_{DR} column intensity in our observed cases in Greensburg, Kansas and Greenville, Texas (Section 4) often exceeded 4.5 dB (Figs. 5 and 9). The default Morrison and Milbrandt (2011) microphysical parameterization scheme in CM1 has an upper limit of 2.8 mm on the mean drop size (H. Morrison, 2025 personal communication). Since 2.8 mm corresponds to Z_{DR} of roughly 4.0 dB (Beard and Chuang 1987), this limit could explain this apparent Z_{DR} upper bound. Furthermore, the drop size distribution tails off exponentially at these large (> 2.8 mm) drop sizes, potentially allowing Z_{DR} to range up to the apparent 4.5 dB limit. The mean drop size parameter could be adjusted in future work to allow for larger drop sizes, and presumably larger Z_{DR} values, in the synthetic radar data.

Bearing this caveat in mind, the Z_{DR} column intensities were still higher overall (3.5 dB to 4.5 dB) for the tornadogenesis cases, particularly prior to tornadogenesis (Fig. 21a). In contrast, Z_{DR} intensities from nontornadic members had a larger spread (2.0 to 4.3 dB). The nontornadic cases exhibited a mean trend of increasing Z_{DR} column intensity three minutes prior to tornadogenesis failure, maintaining this relatively high intensity until two minutes after tornadogenesis failure before decreasing again (Fig. 22a). Due to the apparent artificial 4.5 dB upper bound imposed by the two-moment Morrison and Milbrandt (2011) scheme, however, the tornadic Z_{DR} intensity trends are less clear than those for tornadogenesis failure, in which the Z_{DR} column intensity stayed below the artificial upper bound.

Clearer trends were obtained in the Z_{DR} column area for each tornadogenesis (failure) event (Figs. 21b and 22b). Overall, Z_{DR} column area was larger by a factor of two for tornadogenesis events (Fig. 21b) than tornadogenesis failure events (Fig. 22b). The ensemble mean nontornadic Z_{DR} column area showed relatively small fluctuations (4 km^2) during the 11-minute window centered on tornadogenesis failure (Fig. 22b), and in contrast, the ensemble Z_{DR} column area for the tornadic cases increases by ~5 to 7 km^2 to a mean of 21 km^2 in the two minutes prior to tornadogenesis, indicating a broadening updraft (French and Kingfield 2021; Trapp et al. 2017). The genesis events show more variability in Z_{DR} column area, potentially indicating different levels of organization within the updraft of each storm.

Lastly, we examine the trends in Z_{DR} column height for each tornadogenesis and each tornadogenesis event (Figs. 21c and 22c). Z_{DR} columns at tornadogenesis, on average, increase in height by 1.0 km in the 3 min prior to tornadogenesis events. The tornadogenesis failure events show only minor variations in Z_{DR} column height, with a slight increase in mean height (~ 0.5 km) prior to tornadogenesis failure (Fig. 22c), possibly indicating weaker and/or less organized updrafts. This result is consistent with the lower aspect ratios analyzed for tornadogenesis failure times (Figs. 19 and 20). In contrast, tornadic Z_{DR} column mean heights rose to 2.5 km above the 0 °C level in the two minutes prior to tornadogenesis (Fig. 21c), indicating more vertical development and an intensifying updraft prior to tornadogenesis (Kumjian et al. 2014). As was found with respect to Z_{DR} column area, the tornadogenesis events show more variation in the Z_{DR} column height than do the nontornadic members, indicating different levels of updraft strength for each storm. Despite this greater variability, Z_{DR} columns associated with tornadogenesis have higher aspect ratios (Fig. 19) and interior vertical velocities (Fig. 20) than do their counterparts associated with tornadogenesis failure.

The mean rates of change for each Z_{DR} column metric (intensity, area, and height) were then computed for tornadogenesis (failure) event (Figs. 23 and 24). In the following discussion, intensification rates in the range ±0.2 dB min^{-1} are regarded as "stagnant." Such small changes in Z_{DR} column intensity are unlikely to be operationally detectable, as they fall below calibration limits for most weather radars (Ryzhkov et al. 2005). The second tornadogenesis event in ensemble member

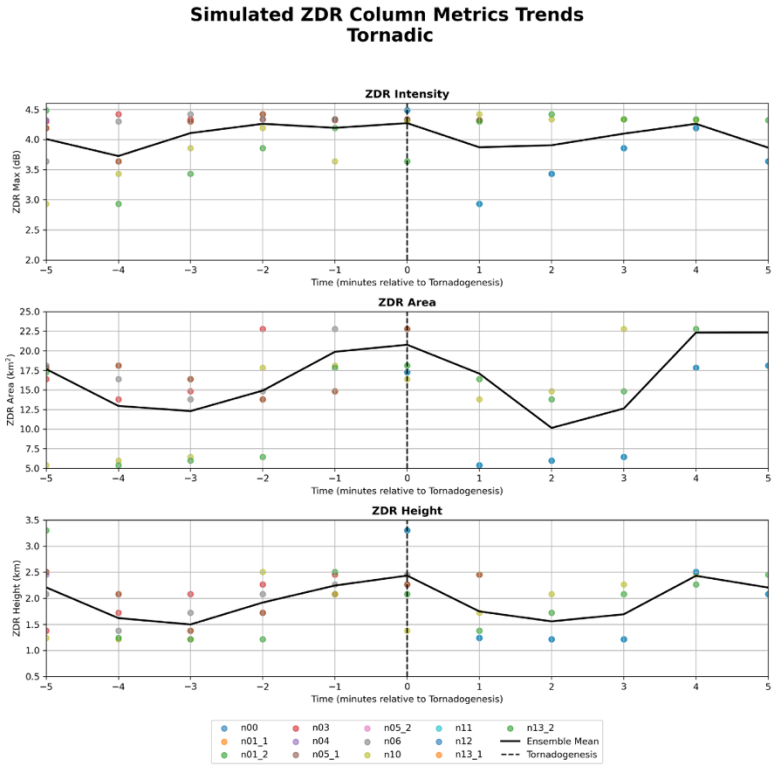

Fig. 21: Z_{DR} column intensity (a), area (b), and height (c) for tornadic ensemble members (colored dots) and their mean (solid black line) Times are given in minutes relative to tornadogenesis.

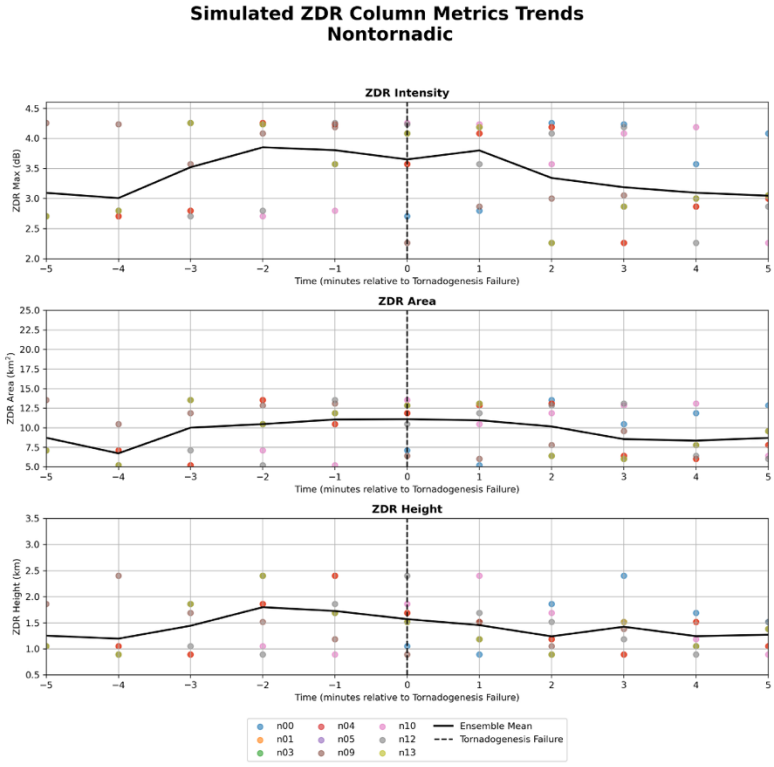

Fig. 22: As in Figure 21, but for nontornadic ensemble members and for times relative to tornadogenesis failure.

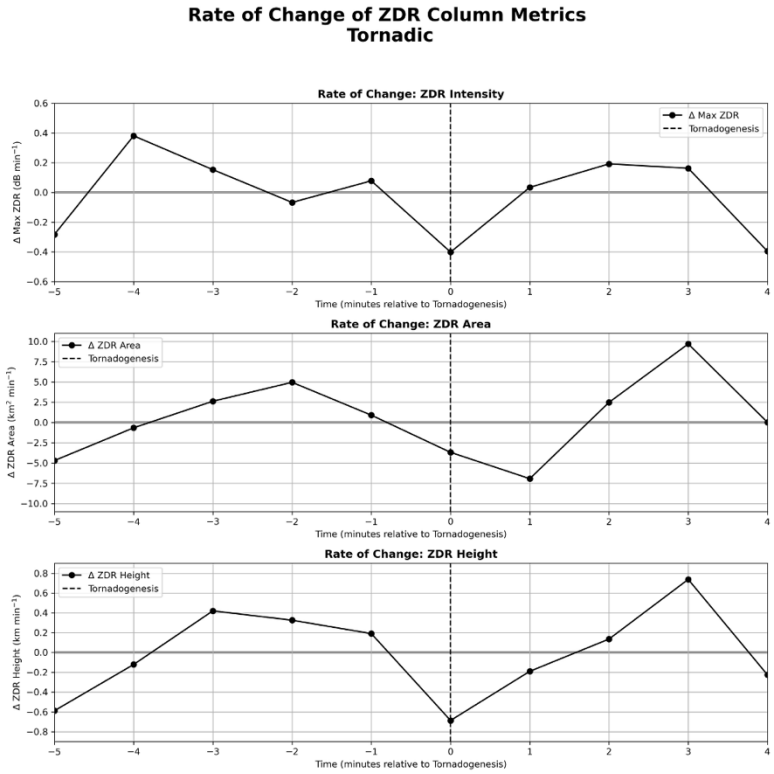

Fig. 23: Rate of change of Z_{DR} column intensity (a), area (b), and height (c) for tornadic ensemble members.

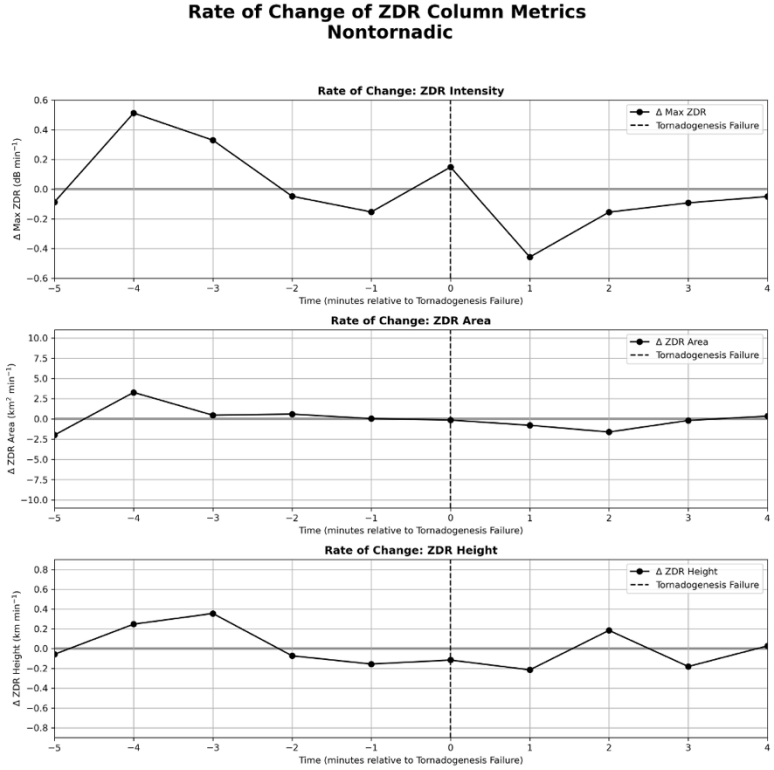

Fig. 24: As in Figure 23, but for nontornadic ensemble members.

tor01 produced a TLV late in the model (at t = 86 min), so the 11-minute time series was padded with NaNs which were then excluded from the rate-of-change calculations.

For both tornadogenesis and tornadogenesis failure events, Z_{DR} columns intensified at a rate of 0.4 to 0.5 dB min^{-1} until about three minutes prior to the event (Figs. 23a and 24a). For tornadogenesis events, the Z_{DR} column intensity stagnated just prior to, and then weakened to -0.4 dB min^{-1} during, tornadogenesis (Fig. 23a). After tornadogenesis, the Z_{DR} column reintensified slightly for two to three min, indicating reinforcement of the updraft.

For tornadogenesis failure events, Z_{DR} columns also stagnated for the two minutes prior to, and during, tornadogenesis failure. Z_{DR} intensity stagnated as tornadogenesis failure occurred, then weakened at a mean rate of -0.4 dB min^{-1} for one minute afterward.

Z_{DR} column expansion rate (rate of change of the Z_{DR} column area) was examined next Figs. 23b and 24b). For tornadogenesis events, the Z_{DR} column consistently expanded at rates up to 5 km^2 min^{-1} in the five to two minutes prior to tornadogenesis (Fig. 23b). The expansion rate then oscillated to negative. Two minutes before tornadogenesis, the mean expansion rate slowed. The column began to contract at tornadogenesis time, contracting most quickly approximately one minute after tornadogenesis (-5 km^2 min^{-1}). Subsequently, the Z_{DR} column expanded again, indicating broadening of the updraft (Fig. 23b). In contrast, in the nontornadic ensemble, the Z_{DR} mean column expansion rate hovered around 0 km^2 min^{-1} during the entire 11-min window, indicating no significant horizontal (or lateral) expansion or contraction of Z_{DR} column area before or after tornadogenesis failure.

Finally, we examined the Z_{DR} column growth rate (rate of change of height (Figs. 23c and 24c). For three minutes prior to tornadogenesis events, Z_{DR} columns grew at rates as high as 0.4 km min^{-1} (Fig. 23c), indicating the updraft was intensifying. The mean Z_{DR} column abruptly shrank by -0.6 km min^{-1} at tornadogenesis time. This result aligns with the hypothesis of Picca et al. (2015), in which the Z_{DR} column was predicted to shrink at tornadogenesis in response to the development of a downward-directed perturbation pressure gradient force in response to the intensifying vortex. The Z_{DR} column resumed growing 2 min after tornadogenesis (Fig. 23c), indicating reintensification of the updraft.

Prior to the tornadegenesis failure events, the Z_{DR} column predominantly shrank (as seen in Fig. 22c). This result, again, suggests overall weaker updrafts in the nontornadic ensemble.

6. Conclusions

In this study, we examined X-band Z_{DR} column metrics (intensity, area, and height) for three observed cases and an ensemble of 30 simulated supercells (half nominally tornadic, and half nominally nontornadic). This study was undertaken to assess whether polarimetric radar observations might be used as a short-fuse predictor of tornadogenesis in supercells. Owing to a paucity of real data sets meeting our selection criteria (rapid volume scans during tornadogenesis and/or tornadogenesis failure), supplementation via simulation was justified.

Our observational data set consisted of only three cases: Two tornadic storm cases, and one apparent tornadogenesis failure case. All of these storms were observed by different X-band radars, possibly having slight differences in calibration. Based on the overall case study results (also summarized visually in Table 4) we conclude:

1. In the Greensburg, Kansas tornadic supercell, an ongoing EF-5 tornado was present through the entire analysis period. Z_{DR} columns exhibited periodic growth (in height) and decay cycles that appeared to lag in at least two satellite tornadogenesis events (Figs. 4, 5), suggesting multiple updraft pulses. However, Z_{DR} column area and intensity did not exhibit consistent behavior with respect to satellite tornadogenesis.
2. In the Luther – Carney tornadic supercell, Z_{DR} column height, area, and intensity all increased rapidly in the four to five min before tornadogenesis (Figs. 6, 7). This behavior suggests rapid growth (and intensification) of the storm's primary updraft prior to tornadogenesis, potentially aiding vortex intensification via stretching, consistent with our hypothesis.
3. In the Greenville, Texas nontornadic supercell, Z_{DR} column height and area also increased prior to tornadogenesis failure, while intensity stayed relatively

steady (Figs. 8, 9). Unlike the preceding two cases, the Greenville storm exhibited a Z_{DR} column split immediately before tornadogenesis failure (a time defined as when low-level azimuthal shear, a proxy for vorticity, reached a maximum in the hook echo region). This Z_{DR} column split suggests some disorganization within the updraft which could be the cause of tornadogenesis failure. In the classic conceptual model of a splitting supercell (Klemp 1987), the storm's primary updraft is split by a competing central downdraft, reducing each surviving updraft's capacity to stretch the vortex.

Overall, similar Z_{DR} column height and area trends were found in these three diverse supercells (multiple tornadic, tornadic, nontornadic) (Table 5). Z_{DR} column height tended to increase in advance of both tornadogenesis (Greensburg Kansas satellite tornadoes 7 through 10, Luther – Carney, Oklahoma tornado) and tornadogenesis failure (Greenville, Texas storm) cases, but also decreased before Greensburg, Kansas satellite tornado 6. Similar results were found for Z_{DR} column areal coverage above the 0°C level (Table 7). In contrast, Z_{DR} column intensity increased in both tornadogenesis (Greensburg, Kansas satellite tornado 6, Luther – Carney, Oklahoma tornado) and tornadogenesis failure (Greenville, Texas storm) cases, but also decreased in others (Greensburg, Kansas satellite tornadoes 7 through 10). **Based on this very small sample, it is therefore proposed that the X-band Z_{DR} column height, area, and intensity are of limited use for prognosing tornadogenesis on time scales of 5 to 0 min.** Repeating this analysis on a larger set of well-sampled Z_{DR} columns will clarify whether these results apply more generally.

Our simulation results offer a modest glimmer of hope for Z_{DR} column prognostic utility, however. Overall, the analyzed 13 tornadogenesis (i.e. TLV genesis) events had higher intensity, broader area, and taller height in the 5 to 0 min prior to tornadogenesis than did the nine instances of tornadogenesis failure. The Z_{DR} column intensity peaked, on average, two minutes prior to tornadogenesis, weakened at genesis, and then intensified again after genesis (Figure 21). In the tornadic ensemble mean, the Z_{DR} column area expanded more quickly just prior to and just after tornadogenesis, indicating a well-organized, rapidly growing updraft. The nontornadic cases showed more stagnant metrics and rate of change in both Z_{DR} column area and height, with decreasing area and height trends prior to tornadogenesis failure (Figures 22 and 24). The presentation of the Z_{DR} column is affected by the chosen volume coverage pattern (Snyder et al. 2015) and volume update time, during which the storm may translate several km. If the entire radar volume is treated as though all of the data were collected instantaneously, translational distortion may manifest as an artificial enhancement of Z_{DR} column height and area due to tilting. This factor was considered in our case selection criteria (volume update times of two min or less). Because RaXPol and UMass Skyler are capable of exceptionally rapid volume scans (~ 1 min or less), this effect is probably not measurable for the Luther–Carney, Oklahoma and Greenville, Texas cases. Tanamachi et al. (2012) found that UMass X-Pol observations of the Greensburg, Kansas tornado did exhibit artificial tilt with height due to storm translation away from the radar. However, this distortion was corrected in the version of the data set used in that and our research.

Our present research has provided a path toward improved understanding of tornadic and nontornadic storms and their Z_{DR} column behavior. Future research directions include gathering more high spatiotemporal radar data collection above the 0°C level inside the updrafts of potentially tornadic storms. As of this writing, the In-situ Collaborative Experiment for the Collection of Hail In the Plains (ICECHIP; https://icechip.niu.edu/) field campaign, which concluded in July 2025, collected C-Band and X-Band radar observations above the 0°C level in multiple tornadic and nontornadic storms. Owing to ICECHIP's focus on hail, with more scans concentrated aloft, ICECHIP radar data are well suited to expand the present study.

We anticipate further results from future studies incorporating more high spatiotemporal resolution observations of Z_{DR} columns, and synthetic Z_{DR} observations using more advanced microphysics schemes. We look forward to future analyses devoted to Z_{DR} columns and other polarimetric signatures that may be useful for predicting tornadogenesis on short time scales.

ACKNOWLEDGMENTS

The UMass Skyler data were collected under NSF grant AGS-1741003 to the second

author. The authors would like to thank Dr. Howard Bluestein of the University of Oklahoma for providing both UMass X-Pol and RaxPol data under NSF grants ATM-0637148 and AGS-0934307, respectively, Dr. Brice Coffer for providing the namelists and initial soundings for the CM1 ensemble, Dr. Milind Sharma for providing the original gridding and Z_{DR} column identification software, Dr. Steve Frasier for providing and maintaining UMass X-Pol and UMass Skyler under NSF grants ATM-0641201 and AGS-1741088, respectively, and Dr. Hugh Morrison of NCAR for his guidance on his two-moment microphysics scheme used for this research. Simulations were performed on Purdue supercomputing resources under NSF grant AGS-2146262 to Dr. Daniel Dawson. Thanks are due to Dr. Daniel Dawson and Dr. Scott Landolt for their guidance and assistance in completing this work as part of the first authors' thesis committee.

REFERENCES

Beard, K. V., and C. Chuang, 1987: A New Model for the Equilibrium Shape of Raindrops. *J. Atmos. Sci.*, **44**, 1509–1524.

Bluestein, H. B., and R. M. Wakimoto, 2003: Mobile Radar Observations of Severe Convective Storms. *Meteorological Monographs*, **30**, 105–105.

____, and M. M. M. French, R. L. R. L. Tanamachi, S. Frasier, K. Hardwick, F. Junyent, and A. L. A. L. Pazmany, 2007: Close-range observations of tornadoes in supercells made with a dual-polarization, X-band, mobile Doppler radar. *Monthly Weather Review*, **135**, 1522–1543.

____, H. B., J. C. Snyder, and J. B. Houser, 2015: A Multiscale Overview of the El Reno, Oklahoma, Tornadic Supercell of 31 May 2013. *Weather and Forecasting*, **30**, 525–552.

____, H., J. Margraf, T. Greenwood, S. Emmerson, J. Snyder, and L. Wicker, 2025: On the Evolution of Cyclonic and Anticyclonic Tornadoes in a Supercell in Kansas. *COMECAP 2025*, COMECAP 2025, MDPI, 19.

Bringi, V. N., and V. Chandrasekar, 2001: *Polarimetric Doppler Weather Radar: Principles and Applications*. Cambridge University Press, 636 pp.

Brown, R. A., V. T. Wood, R. M. Steadham, R. R. Lee, B. A. Flickinger, and D. Sirmans, 2005: New WSR-88D Volume Coverage Pattern 12: Results of field tests. *Weather and Forecasting*, **20**, 385–393.

Bryan, G. H., and J. M. Fritsch, 2002: A Benchmark Simulation for Moist Nonhydrostatic Numerical Models. *Mon. Wea. Rev.*, **130**, 2917–2928.

Chrisman, J. N., and U. S. D. of Commerce, 2012: *Description Document: Supplemental Adaptive Intra-Volume Low-Level Scan (SAILS)*. Radar Operations Center, https://www.roc.noaa.gov/WSR88D/PublicDocs/NewTechnology/Supplemental_Adaptive_Intra_Volume_Low_Level_Scan_Description_Document_Final.pdf.

Coffer, B. E., M. D. Parker, J. M. L. Dahl, L. J. Wicker, and A. J. Clark, 2017: Volatility of Tornadogenesis: An Ensemble of Simulated Nontornadic and Tornadic Supercells in VORTEX2 Environments. *Monthly Weather Review*, **145**, 4605–4625.

____, and M. D. Parker, 2017: Simulated supercells in nontornadic and tornadic VORTEX2 environments. *Monthly Weather Review*, **145**, 149–180.

____, and M. D. Parker, 2018: Is There a "Tipping Point" between Simulated Nontornadic and Tornadic Supercells in VORTEX2 Environments? *Monthly Weather Review*, **146**, 2667–2693.

Dalman, D. M., R. L. Tanamachi, P. E. Saunders, B. L. Cheong, D. Bodine, H. B. Bluestein, and Z. B. Wienhoff, 2018: Cataloging rapid scan observations of ZDR columns in supercells. *29th Conf. on Severe Local Storms*, Stowe, Vermont, American Meteorological Society, P89.

Dawson, D. T., L. J. Wicker, E. R. Mansell, Y. Jung, and M. Xue, 2013: Low-level polarimetric radar signatures in EnKF analyses and forecasts of the May 8, 2003 Oklahoma City tornadic supercell: Impact of multimoment microphysics and comparisons

with observation. *Advances in Meteorology*, **2013**, 13–13.

Fischer, J., J. M. L. Dahl, B. E. Coffer, J. L. Houser, P. M. Markowski, M. D. Parker, C. C. Weiss, and A. Schueth, 2024: Supercell Tornadogenesis: Recent Progress in our State of Understanding. *Bulletin of the American Meteorological Society*, https://doi.org/10.1175/BAMS-D-23-0031.1.

French, M. M., and D. M. Kingfield, 2021: Tornado Formation and Intensity Prediction Using Polarimetric Radar Estimates of Updraft Area. *Weather and Forecasting*, https://doi.org/10.1175/WAF-D-21-0087.1.

Healey, D. J., and M. S. Van Den Broeke, 2023: Comparing Polarimetric Signatures of Proximate Pretornadic and Nontornadic Supercells in Similar Environments. *Weather and Forecasting*, **38**, 2011–2027.

Heberling, W., and S. J. Frasier, 2021: On the Projection of Polarimetric Variables Observed by a Planar Phased-Array Radar at X-Band. *IEEE Transactions on Geoscience and Remote Sensing*, **59**, 3891–3903.

Hong, Y., and J. J. Gourley, 2015: *Radar Hydrology: Principles, Models, and Applications*. 1st ed. CRC Press, 182 pp.

Illingworth, A. J., J. W. F. Goddard, and S. M. Cherry, 1987: Polarization radar studies of precipitation development in convective storms. *Quarterly Journal of the Royal Meteorological Society*, **113**, 469–489.

Knappik and Frasier, J. and S., 2022: *A Literature Review as Related to Development of a Calibration Procedure for Skyler, a Dual-Polarization Planar Phased Array X-band Radar for Precipitation and Severe Weather Forecasting Research*. University of Massachusetts Amherst, https://www.academia.edu/85737424.

Klemp, J. B., 1987: Dynamics of tornadic thunderstorms. *Annual review of fluid mechanics*, **19.1**, 369-402.

Kollias, P., D. J. McLaughlin, S. Frasier, M. Oue, E. Luke, and A. Sneddon, 2018: Advances and applications in low-power phased array X-band weather radars. *2018 IEEE Radar Conference, RadarConf 2018*, Institute of Electrical and Electronics Engineers Inc., 1359–1364.

Kumjian, M. R., and A. V. Ryzhkov, 2008: Polarimetric signatures in supercell thunderstorms. *Journal of Applied Meteorology and Climatology*, **47**, 1940–1961.

____, and A. P. Khain, N. Benmoshe, E. Ilotoviz, A. V. Ryzhkov, and V. T. J. Phillips, 2014: The anatomy and physics of ZDR columns: Investigating a polarimetric radar signature with a spectral bin microphysical model. *Journal of Applied Meteorology and Climatology*, **53**, 1820–1843.

Kuster, C. M., J. C. Snyder, T. J. Schuur, T. T. Lindley, P. L. Heinselman, J. C. Furtado, J. W. Brogden, and R. Toomey, 2019: Rapid-Update Radar Observations of ZDR Column Depth and Its Use in the Warning Decision Process. *Weather and Forecasting*, **34**, 1173–1188.

Lemon, L. R., and M. Umscheid, 2008: The Greensburg, KS tornadic storm: a storm of extremes. *24th Conf. on Severe Local Storms*, Savannah, Georgia, American Meteorological Society, 2.4-2.4.

Majcen, M., P. Markowski, Y. Richardson, D. Dowell, and J. Wurman, 2008: Multipass objective analyses of Doppler radar data. *Journal of Atmospheric and Oceanic Technology*, **25**, 1845–1858.

Mansell, E. R., 2010: On Sedimentation and Advection in Multimoment Bulk Microphysics. *Journal of the Atmospheric Sciences*, **67**, 3084–3094.

Markowski, P. M., and Y. P. Richardson, 2009: Tornadogenesis: Our current understanding, forecasting considerations, and questions to guide future research. *Atmospheric Research*, **93**, 3–10.

____, and Y. Richardson, 2010: *Mesoscale meteorology in midlatitudes*. Wiley-Blackwell 407pp.

Marshall, T. P., D. McCarthy, J. G. LaDue, J. Wurman, C. Alexander, P. Robinson, and K. Kosiba, 2008: Damage survey and

deduction of vortex structure of the Greensburg, KS tornado. *24th Conf. on Severe Local Storms*, Savannah, Georgia, American Meteorological Society, 8B.3.

Morrison, H., and J. Milbrandt, 2011: Comparison of Two-Moment Bulk Microphysics Schemes in Idealized Supercell Thunderstorm Simulations. *Mon. Wea. Rev.*, **139**, 1103–1130.

National Weather Service, 2013: The Tornado Outbreak of May 19, 2013.

Oue, M., A. Tatarevic, P. Kollias, D. Wang, K. Yu, and A. M. Vogelmann, 2020: The Cloud-resolving model Radar SIMulator (CR-SIM) Version 3.3: description and applications of a virtual observatory. *Geosci. Model Dev.*, **13**, 1975–1998.

Parker, M. D., 2014: Composite VORTEX2 supercell environments from near-storm soundings. *Monthly Weather Review*, **142**, 508–529.

Pazmany, A. L., J. B. Mead, H. B. Bluestein, J. C. Snyder, and J. B. Houser, 2013: A mobile, rapid-scanning, X-band, polarimetric, (RaXPol) Doppler-radar system. *Journal of Atmospheric and Oceanic Technology*, **30**, 1398–1413.

Picca, J. C., J. C. Snyder, and A. V. Ryzhkov, 2015: An observational analysis of ZDR column trends in tornadic supercells. *37th Conf. on Radar Meteorology*, Boston, Massachusetts, American Meteorological Society, 5A.5-5A.5.

Radar Operations Center and DOC/NOAA, 2015: *WSR-88D Volume Coverage Pattern Improvement Initiatives*. DOC/NOAA, https://www.roc.noaa.gov/public-documents/engineering-branch/new-technology/vcp/level-two/pdf/misc/New_VCP_Paradigm_Public_Oct_2015.pdf

Rauber, R. M., and S. W. Nesbitt, 2018: *Radar meteorology: a first course*. First edition. Wiley Blackwell 1p.

Romine, G. S., D. W. Burgess, and R. B. Wilhelmson, 2008: A dual-polarization-radar-based assessment of the 8 May 2003 Oklahoma City area tornadic supercell. *Monthly Weather Review*, **136**, 2849–2870.

Rotunno, R., and J. Klemp, 1985: On the rotation and propagation of simulated supercell thunderstorms. *Journal of the Atmospheric Sciences*, **42**, 271–292.

Ryzhkov, A. V., S. E. Giangrande, V. M. Melnikov, and T. J. Schuur, 2005: Calibration Issues of Dual-Polarization Radar Measurements. *J. Atmos. Oceanic Technol.*, **22**, 1138–1155.

Seliga, T. A., and V. N. Bringi, 1976: Potential use of radar differential reflectivity measurements at orthogonal polarizations for measuring precipitation. *Journal of Applied Meteorology*, **15**, 69–76.

Sharma, M., R. L. Tanamachi, E. C. Bruning, and K. M. Calhoun, 2021: Polarimetric and Electrical Structure of the 19 May 2013 Edmond-Carney, Oklahoma Tornadic Supercell. *Monthly Weather Review*, **149**, 2049—2078.

Snyder, J. C., A. V. Ryzhkov, M. R. Kumjian, and J. Picca, 2015: A ZDR column detection algorithm to examine convective storm updrafts. *Weather and Forecasting*, **30**, 1819–1844.

Tanamachi, R. L., H. B. Bluestein, J. B. Houser, K. M. Hardwick, and S. J. Frasier, 2012: Mobile, X-band, polarimetric Doppler radar observations of the 4 May 2007 Greensburg, Kansas tornadic supercell. *Monthly Weather Review*, **140**, 2103–2125.

____, and P. L. Heinselman, and L. J. Wicker, 2015: Impacts of a storm merger on the 24 May 2011 El Reno, Oklahoma tornadic supercell. *Weather and Forecasting*, **30**, 501–524.

____, and M. Sharma, A. T. LaFleur, S. J. Frasier, W. Heberling, C. Wolsieffer, L. Warner, and R. Nelson, 2020: Observations of ZDR Columns in Supercells in 2019 by a Mobile, Dual-Polarized, Phased-Array Radar. Severe Local Storms Symposium, Boston, Massachusetts, American Meteorological Society, P926.

Trapp, R. J., G. R. Marion, and S. W. Nesbitt, 2017: The Regulation of Tornado Intensity by Updraft Width. *Journal of the Atmospheric Sciences*, **74**, 4199–4211.

Van Den Broeke, M. S., 2017: Polarimetric Radar Metrics Related to Tornado Life Cycles and Intensity in Supercell Storms. *Monthly Weather Review*, **145**, 3671–3686.

____, 2020: A Preliminary Polarimetric Radar Comparison of Pretornadic and Nontornadic Supercell Storms. *Monthly Weather Review*, **148**, 1567–1584.

Virtanen, P., and Coauthors, 2020: SciPy 1.0: fundamental algorithms for scientific computing in Python. *Nat Methods*, **17**, 261–272.

Wakimoto, R. M., N. T. Atkins, K. M. Butler, H. B. Bluestein, K. Thiem, J. Snyder, and J. Houser, 2015: Photogrammetric Analysis of the 2013 El Reno Tornado Combined with Mobile X-Band Polarimetric Radar Data. *Monthly Weather Review*, **143**, 2657–2683.

Weber, M., and Coauthors, 2021: Towards the Next Generation Operational Meteorological Radar. *Bulletin of the American Meteorological Society*, **102**, E1357–E1383.

Wienhoff, Z. B., H. B. Bluestein, L. J. Wicker, J. C. Snyder, A. Shapiro, C. K. Potvin, J. B. Houser, and D. W. Reif, 2018: Applications of a Spatially Variable Advection Correction Technique for Temporal Correction of Dual-Doppler Analyses of Tornadic Supercells. *Monthly Weather Review*, **146**, 2949–2971.

Wilson, M., and M. Van Den Broeke, 2022: Using the Supercell Polarimetric Observation Research Kit (SPORK) to examine a large sample of pretornadic and nontornadic supercells. *Electronic Journal of Severe Storms Meteorology*, **17**, 1–38.

Ziegler, C. L., 1985: Retrieval of Thermal and Microphysical Variables in Observed Convective Storms. Part 1: Model Development and Preliminary Testing. *J. Atmos. Sci.*, **42**, 1487–1509.